PREPRINT UCRL-84002

CONF-800208--12

Lawrence Livermore Laboratory

LASER FUSION EXPERIMENTS, FACILITIES AND DIAGNOSTICS AT LAWRENCE LIVERMORE LABORATORY*

Harlow G. Ahlstrom

February 1980

This paper was prepared for submission to Conference on Laser and Electro-Optical Systems, San Diego, Ca.. February 26-28, 1980.

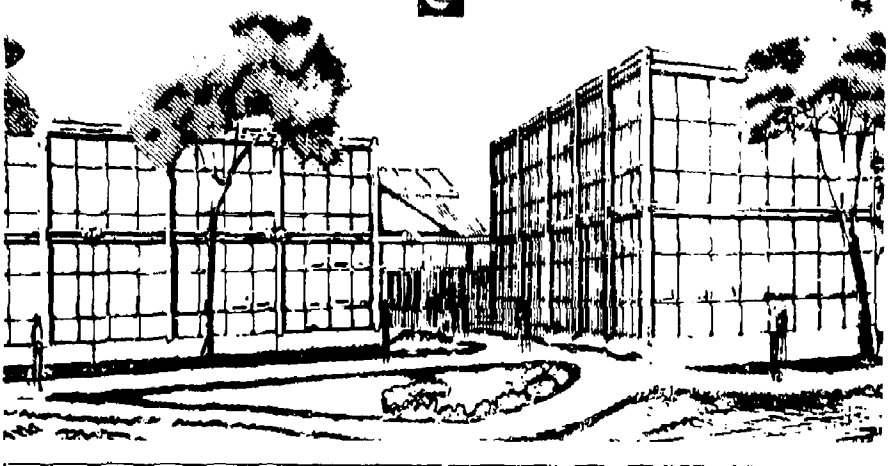

LASER FUSION EXPERIMENTS, FACILITIES AND DIAGNOSTICS AT LAWRENCE LIVERMORE LABORATORY*

H. G. Ahlstrom

University of California, Lawrence Livermore Laboratory
P. O. Box 5508, Livermore, California 94550

ABSTRACT

The progress of the LLL laser Fusion Program in our work to achieve high gain thermonuclear micro-explosions is discussed. Many experiments have been successfully performed and diagnosed using the large complex, 10-beam, 30 TW Shiva laser system. A 400 kJ design of the 20-beam Nova laser has been completed. The construction of the first phase of this facility has begun. The first phase of this Nd doped fluorophosphate laser will consist of ten beams producing 100 kJ in 1 ns pulses. One beam of the Argus laser has been converted to operation at 532 nm with 10 cm aperture. It will soon operate at 355 nm, also at 10 cm aperture. Frequency conversion crystals are being procured for full aperture, 28 cm, operation at either 532 nm or 355 nm for both Argus beams.

We also discuss new diagnostic instruments which provide us with new and improved resolution, information on laser absorption and scattering, thermal energy flow, suprathermal electrons and their effects, and final fuel conditions. We have made measurements on the absorption and Brillouin scattering for target irradiations at both 1.064 μm and 532 nm. These measurements confirm the expected increased absorption and reduced scattering at the shorter wavelength. Additional data has been obtained on the angular distribution of suprathermal x-rays which further confirms our observation of its non-isotropy, however, we do not yet have an explanation of the phenomena.

Implosion experiments have been performed which have produced final fuel densities over the range of 10x to 100x liquid DT density. The 100x achievement is the highest yet achieved in laser fusion DT fuel targets.

*Work performed under the auspices of the U. S. Department of Energy by the Lawrence Livermore Laboratory under Contract No. W-7405-Eng-48.

INTRODUCTION

The laser program at the Lawrence Livermore Laboratory has made significant progress towards the goal of achieving high gain fusion micro-explosions for the ultimate use of producing energy. Due to the small amount of laser energy that was available with our early facilities, Janus and Cyclops, and also due to the developments required in target fabrication to produce necessary target structures, our early experimental program concentrated on a target type which we call an exploding pusher.[1,2,3] These targets were characterized by a thin glass micro-shell filled with deuterium tritium gas. The sizes necessary for our early experiments were in a range of 50-100 μm diameter with a wall thickness of about 0.50-1 μm. With the lasers available, we were able to produce intensities on target of the order of 10^{15} to 10^{16} W/cm^2. Under these conditions the suprathermal electrons, which are produced by the resonance absorption process, had ranges large compared to the target structure. Thus, the energy was deposited essentially instantaneously throughout the shell of the glass target. This produced explosive decompression of the pusher, both inward and outward. The inward motion of the glass plasma compressed and heated the fusion fuel to densities of approximately that of liquid deuterium tritium and temperatures ranging from 0.50 to 10 keV. This type of target is very useful in studying the laser plasma interaction process, the absorption and propagation of the laser energy in the target, for studying the production of thermonuclear reactions in laser irradiated targets and in developing the two-dimensional computer codes which we use to model the laser fusion targets.

This type of target cannot produce the high gains that are necessary for energy production from inertial confinement fusion. High gains will be achieved by compressing the fuel nearly isentropically staying as close as possible to the Fermi degenerate state.[4] We still have to get the fuel to temperatures on the order of 5 keV for it to ignite and efficiently burn the fuel, but we must produce compression of the fuel in a more controlled manner than previously. The explosive decompression of the pusher in the exploding pusher approach produces strong shock heating of the fuel which puts it at a high entropy level. The approach we are now using, or at least approaching, is what we call ablative acceleration of the pusher. In this approach, we apply the laser energy to the outer surface of the target in such a manner that it heats the material to the plasma temperatures and produces a smooth inward push on the target pusher material.

To achieve the desired high gain conditions, we need to have low Z ablators for efficient acceleration of the pusher material. High density and high Z pushers are required both from the point of view of stability of the compression of the fuel and from the point of view of protection of the inner portion of the pusher and the fuel from the preheat effects of suprathermal electrons.[5,6]

For our early exploding pusher targets, we were able to purchase the glass micro-shells from commercial sources. However, for our high density and high gain targets, we have an active program to develop the techniques required to produce multi-layer structures of various materials.[7]

The history of the program in implosion targets and the projections for the future are shown in Figure 1. Here we plot the DT ion temperature in keV

and the quality of inertial confinement in $n\tau \sim cm^{-3}s$. The history of the exploding pushers is shown by the lower path which begins with Janus I at 0.2 TW in 1974. In 1976 on Janus, we made our first attempts at achieving higher densities with targets operating in a more ablative pusher mode. In 1978, the majority of the Argus experiments were devoted to the attempts to achieve higher densities. The Shiva campaign, with 8 kJ available in 1979, achieved a final fuel density of 100x DT liquid density. In 1980, with improvements in target fabrication and the full energy ability of the Shiva system, we hope to approach 1000x DT liquid density. The Nova laser will be required to achieve ignition and scientific breakeven. Reactor targets with gains greater than 100 are projected to require between 1 and 5 MJ of input laser energy.

In this paper, we will discuss our developments in facilities, diagnostics and interaction physics and our implosion experiments. In 1979, it became apparent that shorter wavelength lasers would be important in the future, and that interaction physics problems would be significantly alleviated by using wavelengths shorter than 1 μm. We had planned to do experiments at 532 nm on Janus, but the priority never became high enough for us to implement that plan.

The developments of the krypton fluoride laser and the xenon chloride laser as possible fusion driver candidates made it imperative to get data on the scaling of the laser plasma interaction at shorter wavelengths.[8,9,10] Therefore, we used an available frequency doubling crystal with the south arm of Argus to provide us with a capability of performing interaction experiments at 532 nm.[11] We also purchased additional crystals so that we could frequency triple the output of Argus for experiments at 355 nm. Experiments

with the frequency doubled Nd glass lasers at Garching,[12] Ecole Polytechnique,[13] Rutherford Laboratories[14] and at Livermore,[15] all indicate that the absorption of the laser light is improved and, as expected, the production of suprathermal electrons scales as $I\lambda^2$,[2,2,16,13] thus, reducing the problems with the suprathermal electrons. Brillouin scattering still occurs, however, its effects are also alleviated at the shorter wavelengths.

Our program to design and build the Nova laser fusion facility[17] is continuing, however, there has been one major modification in the plans in the past year. Based on the recommendation of the Foster Committee which reviewed the Inertial Fusion program, the Nova program is now defined in two phases. That is, the first phase of the Nova laser will be constructed as a ten-beam facility,[18] and the second phase will replace the Shiva laser with an additional ten Nova beam lines to bring the facility to the total of twenty beams and approximately 300 kJ output. The facility is being designed in such a way to allow the options to frequency convert Nova to 527 nm or to the blue at 351 nm.[19] The decision concerning the frequency conversion of the Nova beams will be based on additional information that we gather in the next year on the scaling of the interaction physics and the feasibility of implementing segmented crystal arrays while still achieving at least 50% conversion of the laser 1 μm laser radiation to the shorter wavelengths. The present indications are that the improvement in the interaction physics and energy flow in the laser fusion targets for the shorter wavelength is worth the reduction in output energy of a factor of 2. The present Phase I Nova design will produce a minimum of 90 kJ at 1 ns and 110 kJ at 3 ns.

Our Diagnostics Development program has produced a number of important new instruments for use with longer pulse lengths appropriate to the ablatively driven targets. Because of the corresponding increase in the extent of the underdense plasma Raman scattering has become an important consideration.[20] Therefore, on Shiva we are implementing a Raman spectrometer[21] which will allow us to diagnose the extent of the Raman scattering and also use the data as another indication of plasma temperature.

In understanding the energy flow in the laser targets, one of the most important features is the low energy x-ray emission from the thermal plasma. As a result, on Shiva we have implemented two new time resolved low energy x-ray spectrometers: one of them utilizing our x-ray streak camera technology[22] which has a time resolution of 15 psec and the other utilizing windowless x-ray diodes[23] and fast oscilloscopes providing a time resolution of about 150 psec.

Another diagnostic which will be extremely important during the coming year is that of using an auxiliary x-ray source produced by one or more of the Shiva laser beams as a radiographic source for examining the dynamics and symmetry[25] of the pusher in our laser fusion targets. Shiva will soon have synchronous oscillators, one which can be used to provide the target irradiation pulse and the other which can be used with one or more of Shiva's arms to produce the x-ray backlighter source with an independent pulse length.

A Wolter microscope has been fabricated with a spatial resolution better than 2 μm.[26,27] It will be used to image the x-rays from the backlighting source as they pass through the laser fusion target. Film or a CCD array will

be used to record the image in the flash radiographic mode, and one of our x-ray streak cameras will be used to record the time history of the x-rays passing through the pusher when we are examining the pusher time history.

We have also implemented two methods of examining the effects of the suprathermal electrons. The first is an improvement of the optical pyrometer[28] which was utilized in Argus experiments last year. In addition, we have provided crystal spectrometers to look at fluorescent x-rays from the deposition of suprathermal electrons in pusher materials.

Finally, we have made some additional progress in our radiochemistry nuclear activation program.[24,29,30,31] The detector system that we use to examine the activation of the target materials is basically the same as the one which we implemented last year.[32] However, we have now identified additional materials[24,33] which will give us important information both on the pusher areal density and the fuel areal density. The developments here are primarily in our target fabrication program in which we have been able to coat glass micro-shells with copper which will be used to obtain more information about the pusher material at burn time. We have also identified bromine as an extremely useful material with which to seed the fuel and thus determine fuel ρR at burn time.

In our Interaction Physics program, we have obtained important information on the absorption of the laser light, and on the Brillouin and Raman scattering, both at 1 μm and at 532 nm,[34] we have continued to measure the angular distribution of the suprathermal x-rays[24,35] and have obtained additional information on this phenomenon. Measurements on the thermal x-ray emission from disk targets[36] has provided additional information about the energy flow in the laser targets.

Finally, we discuss the diagnostic information and calculations on our 10x liquid density experiments.[24,37,38] The diagnostics of these particular experiments are very extensive, the density having been determined by three independent techniques. The measurements and calculations[39] of these experiments give us further confidence in the results which we obtained on our 100x liquid density experiments.

SECTION II - FACILITIES

The Shiva system[40] which has been used extensively in the last year is our first departure from a two-beam illumination system. The twenty beams of Shiva provide interesting options for illumination geometries, but of course the number increases the complexity of setting up the Shiva beam positions with respect to the target. On the right hand side of Figure 2 we show the twenty Shiva beams arrayed onto a spherical target. In a natural illumination pattern, the inner and outer pentagonal arrays of the Shiva beams are arranged so that the polarization vectors effectively generate a radial polarization of the cluster of ten beams. Of course, by individually pointing each one of the beams any irradiation pattern can be achieved within the constraints of the lens' positions.

In the upper left of the figure is shown a polar grid which represents the hemisphere presented to each of the two opposing clusters of the Shiva beams. In the setup of an experiment, the experimental physicist can utilize the Shiva computer system to generate this grid and designate the locations and sizes of each of the beams on the target.[41]

The lower left portion of Figure 2 shows a Shiva computer system generated display of the intensity distribution for a 20-beam 10x target irradiation. The computer system allows the physicist to specify the location of the individual beams with respect to the target as illustrated in the upper left, and produce the plot of intensity distribution on the target as shown in the lower left.[42]

The Argus laser system has been reconfigured to allow us to do experiments at twice the fundamental output frequency, ($2\omega_L$) 532 nm, and in 1980 it will be configured to do experiments at three times output frequency, ($3\omega_L$) 355 nm.[11] The conversion of Argus in 1979-1980 will be at 10 cm output aperture. The primary reason for this limitation of the aperture was the previous procurement of optics for the conversion of Janus which has an aperture of 8.5 cm. In 1981, we plan to convert the full 28 cm output aperture of Argus to either $2\omega_L$ or $3\omega_L$. The decision on which wavelength will be made based on experiments performed in 1980. The primary goal of the experiments at $2\omega_L$ and $3\omega_L$ are to confirm and understand the coupling physics at wavelengths shorter than 1 μm which will affect the Nova laser fusion facility and the advanced laser driver program.

The south arm of Argus is down telescoped from 28 cm to the 10 cm aperture of the doubling crystal. A type II KDP doubling crystal is used as shown in Figure 3. The converted beam passes through a beam dump which rejects the unconverted ω_L beam. The $2\omega_L$ beam is directed into the target chamber and is focused onto the target with an f/2.2 lens. Another f/2.2 lens is utilized for transmitted beam diagnostics. The incident beam, as in all our experiments, is diagnosed with a near field camera, an equivalent target plane camera, a calorimeter and a streak camera. The energy not absorbed by the target and not passed into the transmitted beam diagnostics or reflected back into the backreflected beam diagnostics is collected by one of our standard box calorimeters. In this way we are able to account for all of the laser energy which is not absorbed by the target and thus produce an accurate determination of that energy which is absorbed by the target. The light

coming back through the focusing lens is partially transmitted through the final turning mirror and is diagnosed by the backreflected beam diagnostics system which consists of a calorimeter, an optical spectrometer, an optical streak camera and two-dimensional time integrated imaging.

The $2\omega_L$ conversion of Argus began operation in December and has been producing data for the Interactions Experiments program since that time. The $3\omega_L$ conversion will take place in June of 1980. In addition, we will examine the operational feasibility of multi-element crystal arrays for large aperture conversion of the laser frequency.[43] A 10 cm aperture four-element array is being fabricated and will be tested early in 1980. This unit will help determine the feasibility of multi-element arrays for operation at the 28 cm aperture of Argus which is planned to be implemented in 1981, and the feasibility of multi-element arrays for Nova at 74 cm aperture. 15 cm aperture single crystals are presently available which could be used for the 28 cm aperture implementation of Argus, and it is expected that larger aperture crystals can be grown so that, possibly, four-element arrays could be utilized with Nova.

The staging of the Nova laser has been specified in 1979. The Foster Committee,[44] which was charged with reviewing the status and future of the Inertial Confinement Fusion program in the United States, recommended to the Department of Energy that Nova proceed in two phases. The first phase is to consist of half of the total system at a total cost of $136 million. Nova Phase I will occupy the new Nova building which is presently under construction and is connected to the Shiva building. It has been determined that fluorophosphate glass is the best candidate for the Nova output

amplifiers.[18] The reduced non-linear index of refraction allows higher peak power performance than could be obtained with silicate glass, and the high saturation fluence produces the most energy for pulse lengths greater than 1 ns. A decision which has still not been made is whether or not to use fluorophosphate or simple phosphate glass in the smaller diameter amplifiers for the Nova system.

Figure 4 shows the staging of the Nova system. Ten beams of the Nova system will be implemented in Nova Phase I. The system will utilize Shiva hardware up through the 14.5 cm disk amplifiers. However, of course the glass will be changed from silicate to either phosphate or fluorophosphate glass. The 20.8 cm, 31.5 cm and 46 cm disk amplifiers will be of the new high efficiency, so called "box amplifier" design.[45] The 20.8 cm and the 31.5 cm aperture disk amplifiers will utilize longitudinal flash lamp configurations whereas the 46 cm aperture disk amplifier will utilize a transverse flash lamp configuration. Figure 4 shows four of the 31.5 cm aperture amplifiers and three 46 cm amplifiers. Two additional amplifiers of both apertures are shown dashed in the figure. These amplifiers can be added in the future to increase the laser output if more money is available and higher damage threshold coatings are developed so that the higher fluence levels can be used. The Nova system utilizes disk amplifiers, Faraday rotation isolation stages and spatial filter image relay systems.[46] The hard aperture at the beginning of each one of the amplifier chains is imaged through the laser system to the input of each succeeding spatial filter lens and from the final output spatial filter to the target focusing lens. The use of this image relaying concept

has proved essential in the operation of both Argus and Shiva and is a fundamental concept which must be utilized in any high power laser system for either fusion experiments or for a power reactor.

Figure 5 shows the energy and power capability of the present Nova design based on two assumptions with respect to damage thresholds of bulk and anti-reflection coated surfaces. The lower limit presented, the so called "A" fluence limit, is based on current median damage thresholds which are achieved in our present systems. At 1 ns this corresponds to damage thresholds of 5 J/cm^2 on anti-reflection coatings and 16 J/cm^2 for bulk damage. The "B" fluence limit corresponds to the damage thresholds for best of today's available surfaces. At 1 ns on anti-reflection surfaces this corresponds to 8 J/cm^2 and for bulk damage 19 J/cm^2. Thus, at 1 ns based on these existing levels and projections the Nova system would produce between 86 and 100 kJ. At 3 ns the range would be from 107-131 kJ for Phase I of Nova.

Because of the high payoff in terms of system capability for higher damage limit surfaces, our Solid State Laser program is conducting an intensive program to understand the phenomena which lead to damage of optical surfaces and to improve the damage resistance of the surfaces. In a number of cases, we have already seen an improvement of the anti-reflection coating damage threshold at 1 ns to greater than 12 J/cm^2. If these improvements can be implemented on a production basis, there is a possibility that the output of the Nova system could be increased by as much as 50% over the "B" fluence level. These improvements, of course, would also require the addition of the amplifiers shown in Figure 4. The full Nova system, or Phase II of Nova, then has the potential of being able to produce as much as 400 kJ in a 3 ns pulse.

The Nova Phase I irradiation configuration is still being defined. However, it has been decided that there will be two clusters of five beams from each side. The enclosed cone angle of the pentagonal arrays is still to be determined. The present Nova building configuration allows this angle to be varied from 80-110^0.

Figure 6 shows an artist's conception of the Nova Phase I target chamber with the pentagonal beam clusters arranged in the 110^0 included angle configuration. The focusing lenses are f/3. In the 110^0 included angle configuration, the focusing on a spherical target is equivalent to a twelve-beam dodecahedral irradiation system.

In Figure 7, we show the intensity pattern which would be produced on a spherical target in this configuration.

SECTION III - DIAGNOSTICS

In the present organization of the Fusion Experiments program, the major responsibility for fielding and planning the experiments is with the Experiments group. The Laser Fusion Diagnostics group has the primary responsibility for x-ray and particle diagnostics. The Experiments group still maintains the expertise and fielding of optical diagnostics. Also, we have the Diagnostics Development group which is responsible for the long term development of new diagnostics instruments and technologies for our fusion experiments. In this section, I discuss contributions from all three of the above mentioned groups.

In the last year we have become much more interested in the question of Raman scattering from our laser fusion targets,[20] both from the point of view of providing additional diagnostic information on the plasma temperature, but also with respect to the energy balance in terms of the energy coupled to the laser target.

The obvious signature of Raman scattering is the $2\lambda_L$ light backscattered from the laser target. This presents a particularly interesting challenge since this light is at 2 μm. Detectors certainly exist for this wavelength range, but they are beyond the range that we normally operate in with our 1 μm lasers.

In Figure 8 we show the optical configuration which will be used with Shiva to collect 2 μm scattered light from the laser target, an infrasil vacuum window with appropriate filters and 1 μm blocking filter will be mounted on the target chamber. An aluminum mirror will direct a portion of

this light to an ellipsoidal focusing mirror which will focus the light onto a 1 mm diameter ultra high purity quartz single optical cable. This cable will conduct the Raman scattered light to the Raman spectrometer shown in Figure 9. The light from the cable will be incident on a parabolic mirror which directs the light to 300 lines/mm grating which is blazed for ? μm. The spectrally dispersed light from the grating is then focused with a parabolic mirror onto the 36-element array indium arsenide detectors which are cooled to 77^{0} K. This system will then allow us to make spectral measurements of the Raman scattered light from the target.[21] The spectrum will provide additional information about the plasma temperature and the interaction processes.

In understanding the energy flow in our fusion targets, one of the most important emissions which can be diagnosed is the thermal x-ray emission from the target. Typical temperatures at the ablat on surface where most of the x-ray energy is emitted are in the range of several hundred eV to 1 keV. Thus, it is extremely important to be able to measure the sub keV x-ray emission from the laser irradiated targets. Our first approach to making these measurements was to use crystal spectrographs. Previously, we have reported on lead sterate and lead mirastate crystal spectrometers and the data which we have obtained from them. However, this data was time integrated, and as we have shown so many times, time resolved information is much more useful and less ambiguous for understanding processes occurring in the targets. Last year, we reported on our ten-channel Dante spectrometer which utilizes windowless x-ray diodes and filters. The diodes are fast response detectors which when coupled to fast oscilloscopes and provide temporal resolution of

the order of 100-500 psec. The difficulty with this system is that for spectra whi oeak at several hundred volts, the spectral definition below that peak is very poor. To alleviate this problem, on Shiva we have implemented a five-channel mirror Dante arrangement[23] as shown in Figure 10. The addition of a critical angle reflection mirror eliminates the unwanted response of the detector system above the L or K-edge of the filter.

A typical mirror Dante channel is shown in Figure 11. The glass shield protects the calibrated prefilter, the x-rays after passing through the collimator, the debris shield and the filter reflect at a grazing incidence angle from a carbon or beryllium mirror. The reflected x-rays then contain only energy below the critical angle reflection of the mirror, these x-rays are then incident on the windowless x-ray diode. Two versions of the detector have been used: one which has a temporal response of several hundred psec, and another which has a temporal response of 50 psec. In combination with the Thompson CSF-TSN 660 oscilloscope, the 50 psec detector[47] produces a channel with a temporal response of approximately 100 psec. The spectral responses of the five-channel mirror Dante system on Shiva are shown in Figure 12. As indicated in this figure, the utilization of this system will allow us to define the spectral distribution of the x-ray emission from the target in the range of 100 eV to 800 eV.

We have also implemented our streak camera with a very thin carbon window and either Au or CsI for the cathodes. This system is operated in a differentially pumped mode so that the thin carbon window is never exposed to atmospheric pressure. The use of this cathode substrate allows us to extend the operation of our streak cameras down to 200 eV. Last year we operated one of these systems in a three-channel configuration on Argus. However, the

problem that existed at time was that we had not been able to provide an absolute intensity calibration to the system. The system which is now mounted on Shiva[22] has been absolutely calibrated using the Monojoule Laser Facility to produce the x-ray source and using our Dante detectors to absolutely measure the x-rays from the target while simultaneously making the measurement with the soft x-ray streak camera.[48] This has allowed us to provide an absolute calibration of the soft x-ray streak camera spectrometer which is shown schematically in Figure 13. The system as mounted on Shiva utilizes a pinhole for spatial discrimination, critical angle reflection mirrors for high energy spectral discrimination, and a filter pack to provide seven channels of low energy x-ray spectral information. A direct thru-channel will provide correlation of the thermal x-rays with respect to the suprathermal x-rays. The channel response functions are shown in Figure 14. As is indicated, we get channel responses from approximately 200 eV to 900 eV. This system has also been implemented utilizing a CCD array to record the time dependent information in a digital format.[49] As with our other x-ray streak cameras, the temporal resolution of this system is 15 psec.

The combination of the Dante instruments with a soft x-ray streak camera provides us critical instrumentation with which to make vital measurements on the energy flow in our laser fusion targets.

Most of the measurements that we make on our laser fusion targets are made with either self-emission from the target or scattering from the target. A notable exception to this has been the use of an auxiliary probe beam at $4\,\omega_L$ to measure Faraday rotation of the probe in the target plasma or to produce holographic interferograms of the plasma density distribution.[50]

An extension of this concept is to use an auxiliary x-ray source to probe the target structure. For several years we have been developing methods to effectively utilize the concept of x-ray backlighting.[24] The first requirement is that an auxiliary x-ray source have sufficient intensity and short enough wavelength to effectively probe the target structure. Basically, the concept can be used in two ways: one in which a pulse long compared to the target dynamics is utilized and a time resolved recording technique is used to provide temporal information; the second is to provide a means of producing a flash x-ray source which is short compared to the time motion of the target and thus record a flash radiograph of the target structure. To utilize this process we must provide the auxiliary x-ray source, x-ray optics with sufficient collection capability and resolution to be of use and the means of recording the information.

Our X-ray Diagnostics program has been working on each of these problems along with our Solid State Laser program which has addressed the issue of providing a separate time controlled pulse with which to generate the auxiliary x-ray source. We now have available synchronous oscillators[51] so that we can generate either a long pulse separate from the irradiation pulse to provide a x-ray backlighting source throughout the target implosion history or to provide an extremely short, say less than 15 psec, synchronous coordinated pulse[52] to provide a flash x-radiography capability. We have already utilized Fresnel zone plates in the coded imaging mode to record high resolution, $\sim$1 μm, x-ray images and we are continuing to develop Fresnel zone plate structures as x-ray imaging elements.[53] In addition, we are developing artificial crystal structures as efficient x-ray reflecting

elements.[54] On the Shiva system we are installing a 22x magnification Wolter x-ray microscope which has a demonstrated resolution of less than 2 μm.[27] The implementation of this system is shown in Figure 15. Its first intended use will be in resolving pusher dynamics where the recording instrument is one of our soft x-ray streak cameras. In this implementation, the backlighting source will be a long duration source with the time resolution being provided by our 15 psec x-ray streak camera. The x-ray streak camera has a resolution of 100 μm in the film plane, thus, with the magnification of 22 provided by the microscope we obtain a system resolution of 4 μm.

As mentioned previously, the source is as important as the recording element and the imaging element. In Figure 16 we show the results of a series of experiments to determine the feasibility of various materials as x-ray emitters to produce the backlighting source.[55] Titanium, nickel and zinc targets were irradiated at intensities from 3×10^{15} W/cm^2 to 3×10^{16} W/cm^2. What has been shown is that we can obtain a significant fraction of the laser energy in intense helium-like x-rays from these targets. As shown in the figure, we are able to convert almost 0.1% of the laser energy into the helium-like x-ray lines which will be very useful as backlighting sources for our laser fusion targets.

Another area of significant interest is the question of the number and distribution of suprathermal electrons produced in our laser fusion targets. There is not only the question of the number and the distribution, but also how they affect the preheating of the materials in our targets. In Figure 17

we show implementation of the Shiva optical pyrometer[28] which is similar to that used on Argus in 1979. The basic concept is that as materials are preheated by suprathermal electrons, they emit optical radiation which can be recorded. Typically, we expect to have to restrict the preheat temperatures to the order of 1 eV for the pusher and fuel materials in our high density, high gain targets. At these temperatures, the targets are emitting optical radiation which can be detected and recorded by our optical streak cameras.

Figure 17 shows the Shiva optical pyrometer for the detection and recording of preheat signals in pusher materials. The preheat emission from the target is collected and directed to the pyrometer where the beam emitted by the target is split into two channels, filtered to produce two different bands of wavelength beams and focused onto the slit at one of our S-20 photocathode streak cameras. An optical fiducial is produced by taking a portion of the laser beam and converting it to $2\omega_L$ and also putting this signal on the slit of the streak camera.

In 1979 a similar system on Argus was used to record preheat signals on various disk materials irradiated by the Argus laser system.[56] We will soon be using the Shiva system to obtain the same type of information which will provide significant understanding on the effects of these suprathermal electrons in producing preheat in our targets.

Another approach to understanding the effects of the suprathermal electrons is to utilize $K\alpha$ line x-ray emission from cold materials in structured targets. Figure 18 shows conceptually the use of composite targets to study the number and energy distribution of high energy electrons. We will be using this technique with crystal spectrometers to examine the effects of

suprathermal electrons on laser irradiated targets. In the future, we also plan to implement crystal spectrometers with our x-ray streak camera as the recording instrument. This will then provide time resolution on the preheat signal as well. The optical pyrometer and the Kα x-ray spectrometer system will provide significant new information about the effects of suprathermal electrons.

In 1979 we utilized neutron activation of the silicon in our glass pushers as a diagnostic of the areal density of our implosion targets. Through simple models[24,57] or LASNEX calculations,[39] we were then able to relate the areal density measurements of the pusher to the fuel density. We have since identified a number of interesting candidate materials for further diagnosis of areal density of pushers, and even more importantly the areal density of the fuel.[33]

Table I shows the parameters of interest for three materials for our targets. Silicon and copper are materials which can be utilized in the pusher. Bromine is an extremely attractive material which could be added to the fuel to measure the areal density of the fuel. Silicon occurs naturally in our glass micro-shells. As indicated in the table, a $\rho\Delta R$ x yield product of 2×10^4 is sufficient to make a pusher areal density measurement using the silicon. The interpretation of fuel density from the pusher areal density measurement is model dependent. It would be very useful to be able to make the $\rho\Delta R$ measurement of the pusher over several ΔR regions. Copper with its high cross section for activation by 14 meV neutrons is a very interesting candidate to augment the Si measurement. As shown in the table, a $\rho\Delta R$ x yield

product for the copper requires a value of 1.5×10^4, thus, it is in the same range as measurements we have already made with our glass pushers. Our Target Fabrication group has recently demonstrated the capability of coating glass micro-shells with copper[58] with a uniformity and smoothness that is appropriate to our 10-100x targets. This capability will make possible simultaneous $\rho\Delta R(Si)$ and $\rho\Delta R(Cu)$ measurements.

However, our primary requirement is to make a direct areal density measurement of the fuel so that questions of modeling either from simple considerations or LASNEX are not involved in the interpretation. We have identified that bromine is a highly desirable candidate as a seed material in the fuel for this kind of measurement.[33] It has an activated component from the 14 meV neutrons which has an attractive half life, a very high cross section for activation and appears to be one of the most attractive posssibilities for a neutron activation measurement of fuel areal density. The value of ρRP_T, where P_T is the partial pressure, required to make the measurement is 3×10^4. Recently, our Target Fabrication group has demonstrated that they can produce glass micro-shells appropriate to our 10x target achievements with a pressure of 0.4 atm of bromine in the glass micro-shell.[59] This then translates to a yield requirement of 7×10^7 neutrons which is less than the yields achieved in our 10x targets. The glass micro-shells which have been produced with this 0.4 atm of bromine are now being filled with deuterium tritium. Thus, experiments on the direct fuel ρR measurements will be possible in the near future.

To measure the areal density of the fuel in 100x targets will require a yield of approximately 10^7. This is beyond the yield presently achieved, but maybe within reach of experiments later in 1980.

Both ^{62}Cu and ^{78}Br are positron emitters. The same detector system which was used for the activated aluminum counting from the silicon pushers will be utilized for the copper and the bromine detection. Figure 19 shows the positron detection scheme.[33] The copper or the bromine emits a positron which will be collected and detected by the beta fluor. The positron then anihilates and produces two 511 keV gamma rays which will be detected in the NaI gamma detector. The overall detection efficiency for our well counter will be 54% of copper and 51% of the bromine.

We have continued to develop many new instruments and capabilities. Those discussed here are considered to be very important, but they do not represent a comprehensive discussion of our diagnostics development efforts over the last year.

SECTION IV - LASER PLASMA INTERACTION EXPERIMENTS

Over the last year there has been a re-intensification of interest in both lower intensity target irradiations at 10^{13} to 10^{14} W/cm^2 and longer pulses than had been used in early target irradiations associated with exploding pusher targets. Also laser plasma interaction data with the shorter wavelengths which are produced by rare gas halide lasers has become essential to future program planning.

Data for neodymium glass lasers at several nanoseconds obtained at Livermore,[15] the Naval Research Laboratory,[60] and at the Ecole Polytechnique,[13] have shown that absorptions of 60-80% can be obtained on low Z targets. Some of this data is shown in Figure 20. On high Z elements at pulses of the order of a nanosecond, Livermore has demonstrated that absorptions of 50% of the incident laser energy are possible. Recent Argus experiments at 600 psec with frequency doubled neodymium laser light have demonstrated absorptions of approximately 80%. Experiments at Ecole Polytechnique with frequency quadrupled neodymium laser irradiation, also at intensities of 10^{14} W/cm^2, have demonstrated absorptions of as high as 90%. However, this data has been obtained at pulse lengths of 60 psec. Although much data still remains to be obtained to complete our understanding of absorption phenomena as a function of laser intensity and pulse length and laser wavelength, the trend is certainly clear that for intensities of the order of or below 10^{14} W/cm^2, pulse lengths of the order of several nanoseconds and wavelengths ≤ 0.5 μm promise to deliver target absorption in a range of 70-90%.

These optimistic absorption numbers certainly reduce the laser energy required to produce the necessary high gain fusion micro-explosions required for reactor applications. To examine the effects of Brillouin and Raman scattering and transport of energy, we have found it very useful to perform target irradiation at several angles of incidence. The Argus 2 ω_ℓ program involves target irradiation at 600 psec for both low and high Z materials; we have used CH and Au, irradiated in P polarization at 0^0, 30^0, 45^0 and 60^0 angle of incidence with respect to the target normal. The absorption results are shown in Figure 21. As previously noted, the irradiations at 2 x 10^{14} W/cm^2 and normal incidence have produced an absorption of 80%. This result is basically unaffected by rotation of the target by 30^0. Targets irradiated at 1 μm under similar conditions produced absorptions of about 50%.

Figure 22 shows data previously recorded on the spectrum of the light backreflected through the focusing lens on Argus for irradiations at 1 μm. The data are presented for both 3 x 10^{14} W/cm^2 and 3 x 10^{15} W/cm^2. Previously, this data has been interpreted as definite evidence of Brillouin scattering being the primary mechanism for the reflection of the laser light from the target. In addition, if we make the assumption that the plasma dynamics is not significantly affected by the tilt of the target, then one can separate the Doppler shift of the backreflected light due to the outward motion of the underdense plasma and the Brillouin shift. At the lower intensity of 3 x 10^{14} W/cm^2 this then leads to an interpretation of the data which implies a plasma corona temperature of 5$\pm$ 3 keV. At the higher intensity of 3 x 10^{15} W/cm^2, the increased Brillouin shift implies a corona temperature of 20$\pm$ 10 keV.

The Argus data for the 532 nm target irradiations on gold disks at 3×10^{14} W/cm^2 is shown in Figure 23.[15] The backreflected spectrum is shown for normal incidence 45^0 and 65^0 tilt targets. The spectra again are all red shifted indicating that the mechanism for the backreflection of the incident laser irradiation is Brillouin scattering. We also irradiated CH disks at 3×10^{14} W/cm^2 with our frequency doubled output of the Argus laser. The data for the spectrum backreflected through the focusing lens for these targets at normal incidence and 45^0 tilt are also shown in Figure 23.

Now although we still have a significant component in the spectrum shifted to the red indicating Brillouin scattering, we also have a significant portion of this spectrum blue shifted indicating a higher outward velocity of the plasma in these low Z target irradiations. It is probably clear that the plasma conditions obtained at the different tilt angles are in actuality different. However, if we make the simple assumption that the plasma conditions are the same for various tilt angles as those obtained at normal incidence, then we can find the Mach number and the plasma electron temperature where the Brillouin scattering is occurring. Clearly these must be very average numbers, but they do provide interesting insights into the plasma physics phenomena. If we utilize the data at normal incidence and 60^0, we imply a plasma velocity of 2.9×10^7 cm/s with a Mach number of 0.79 and a plasma temperature of 5.5 keV. If we utilize the data at normal incidence and 45^0, then we imply milder conditions; that is, a plasma velocity of 1.8×10^7 cm/s with a Mach number of 0.69 and a electron plasma temperature of 2.8 keV. The variability of these results indicates that

Brillouin scattering is occurring over a wide range of densities, that there is not an invariance of the plasma conditions as we change the incidence angle over a wide range, and that the plasma physics phenomena are quite complicated.

Over the past year, with the realization of the growing importance of Brillouin scattering at long pulse lengths and large target sizes, we have also come to appreciate the possibility of significant Raman scattering of the incident laser beam. Brillouin scattering is the reflection of the incident laser light from ion plasma waves. Raman scattering is the reflection of the incident laser light from electron plasma waves. Raman scattering does not appear to be as important as Brillouin scattering at low densities in the plasma corona, however, at the quarter critical density for the incident laser wavelength, Ncr/4, Raman and the two plasmon decay instability can become very strong.[20] If there is significant plasma in the region of Ncr/4, it is possible that the Raman scattering could play a significant role in the energy balance of laser fusion targets. In addition, it can play a diagnostic role in determining the plasma temperature in the region where the Raman scattering is effective. Raman scattering cannot occur at densities significantly greater than Ncr/4 because the scattered light wave is imaginary. However, there is a small increase in the wavelength beyond 2 λ_L which provides a temperature diagnostic for the plasma at Ncr/4. The cutoff frequency for the Raman scattered light is given by the following equation:

$$\left(0.5 - \frac{\omega_R}{\omega_L}\right)_{max} = \frac{9}{4}\left(\frac{kT_e}{m_e c^2}\right)$$

As indicated by the equation, the maximum frequency is reduced from the half frequency point by the plasma temperature. Thus, the maximum wavelength observed in Raman scattering is increased as a function of the plasma electron temperature. As mentioned in the diagnostic section of this report, we have developed a Raman spectrometer to allow us to measure the spectrum of the Raman scattered light on a single experiment. As a demonstration of the importance and usefulness of measuring the Raman scattered light, we implemented a single detector with band pass filters to measure a portion of the Raman scattered light on individual experiments.

Figure 24 shows data obtained on a series of experiments where we have varied the Z of the material in an attempt to measure the x-ray emission loss from various Z targets. Figure 24 shows the composite Raman spectrum representative of three different Z targets. The data indeed does show that wavelengths greater than $2\lambda_L$ are produced in the scattering process. These experiments were conducted at intensities 3×10^{14} W/cm^2 and, therefore, a small amount of Raman scattered light is anticipated.

Figure 25 shows data for much higher intensities, 10^{16} and 10^{17} W/cm^2, which show orders of magnitude increase in the Raman scattered light. A series of Argus experiments were also done at pulse lengths of approximately 100 psec to examine the inhibition of energy transport into structured disk targets. The data shown in Figure 26 was also obtained for this series and again shows rather minimal levels of Raman scattered light. It does, however, again demonstrate that the cutoff wavelength is greater than $2\lambda_L$. These data convince us that on upcoming Shiva experiments we will obtain additional information on the plasma electron temperature.

We have continued to study the production of suprathermal electrons via our high energy x-ray diagnostics. In code calculations of the production of the high energy x-rays, it is assumed that the high energy electrons are produced isotropically. If this assumption is correct, the production of high energy x-rays from a laser fusion target would be isotropic except for the effects of self-absorption by the target material. As shown in references 24 and 35, angular distribution of the high energy x-rays from a target has been demonstrated to be not isotropic. These measurements were made with a detector filtered with a copper filter, thus, producing response above 50 keV. These measurements have subsequently been confirmed and they continue to show variations in the polar angular emission of the x-rays from laser irradiated targets.

Figure 27 shows the polar distribution of x-rays emitted by gold disk targets irradiated with single beam illuminations of the Shiva system. The intensities on target were typically 2×10^{15} W/cm^2. The polar angle shown in Figure 27 is measured with respect to vertical. The shots labeled beam 13, 11 and 17 were taken with the single beam shots using the upper beams of Shiva. The data designated beam 3 was taken using the beam diametrically opposed to beam 13, thus, from the lower side of the disk. In all cases the target was placed in the center of the target chamber and normal to the centerline of the Shiva beam clusters. The data for beams in the upper cluster produce a higher peak emission on the upper side of the disk than on the lower side of the disk. The opposite is true for the irradiation with

beam 3 where the lower side of the disk produces a higher peak emission than the upper side of the disk. However, the difference between the peak emission on the upper side and the lower side is not as large as those cases for irradiation of the disk with one of the upper beams.

As described in References 24 and 35, the data presented in Figure 27 has been obtained utilizing filtered x-ray diodes. The deficiency of this approach is that it provides a small finite number of data points in the angular distribution. To alleviate this deficiency, we have built a cylindrical film holder which is positioned around the target. The axis of the film cylinder is aligned with the Shiva beam clusters centerline. Thus, the 30.5 cm long 22.9 cm diameter film cylinder does not interfere with the target irradiation and produces the maximum spatial coverage. This will allow us to examine more completely the uniformity of the emission as a function of both the polar and azimuthal angles. This detection system has not yet been used on target experiments. However, to determine the proper exposure levels, we have utilized a plane film pack oriented normal to the target plane.

In Figure 28, we show the illumination orientation of the ten Shiva beams with respect to the disk target which produced an average target intensity of 2.8×10^{14} W/cm^2. A color representation of the x-ray film exposure is shown in the center of the figure again clearly demonstrating the non-uniform polar distribution of the high energy x-ray emission. The data obtained in this figure was filtered with a copper filter again producing the primary response at x-ray energies of 50 keV. The lower polar angles from the disk

exhibit significantly decreased emission, but again demonstrating a peaking of the emission away from the target surface. The reason for the polar non-uniformity of the high energy x-ray emission from the disk is still not explained and remains a subject of intensive investigation in laser plasma interaction experiments.

In addition to this question of the energy and angular distribution of high energy electrons in the laser fusion targets, we are also significantly concerned with the transport of thermal energy in targets where with high Z elements, local thermodynamic equilibrium calculations of the target plasma indicates that a significant fraction of the absorbed laser energy will be radiated away as low energy x-rays. As shown previously for high intensities and short pulse lengths, LTE plasma dynamics does not apply. As we decrease the incident laser intensity and increase the pulse length, non-LTE effects should become less important. These effects are shown in Figure 29 where we plot the radiation loss divided by the absorbed energy and the radiation loss divided by the incident laser energy as a function of incident laser intensity and for two pulse lengths, 1 ns and 2 ns. As predicted by calculations which appropriately take into account non-LTE effects, we see an increase in the radiation loss as we decrease the intensity and also as we increase the laser pulse length. These measurements also indicate that the plasma dynamics become more classical as we increase the pulse length and decrease the incident laser intensity on the target. These effects indicate that as the target scale lengths increase, it may be possible to calculate target performance using classical plasma phenomena without invoking inhibited transport and non-LTE effects.

Figure 30 presents additional data which are highly suggestive of the effects of inhibited transport on a series of experiments at average intensities of 5×10^{14} W/cm^2 with a pulse length of 1 ns FWHM.[36] We utilized one of our Dante channels with the 4 GHz bandwidth oscilloscope to observe the time dependence of the x-ray emission at 0.5 keV. The data shown in Figure 30 show the emission at this x-ray energy as a function of time for U, Au, Sn, Ti and Be targets irradiated under identical conditions. For the U target, the x-ray emission appears to represent a Gaussian distribution in time. For the Au target, it appears that the pulse is approximately Gaussian except in the region of the temporal peak. For Sn and Ti, the distortion from a Gaussian pulse is significant with the Ti data showing very clear evidence of a temporal blocking of the radiation emission. For Be, the effect is so strong that the FWHM of the x-ray emission is almost a factor of 2 greater than that of the laser pulse. The effect is also shown in Figure 31 where we compare the emission from two Au disk targets where we changed the intensity on target by a factor of almost 7.

At 5×10^{14} W/cm^2 as shown previously in Figure 30, there is a change in the approximately Gaussian behavior of the x-ray emission near the peak of the pulse. However, for the target irradiated at 3×10^{15} W/cm^2, the distortion from a Gaussian temporal behavior of the x-ray emission occurs much earlier in time. From this data it appears that as the intensity of the beam on target continues to increase that there is a blockage of energy flow into the high density region of the target and thus the emission of the thermal x-rays. This data has been interpreted as a signature of thermal inhibition.

SECTION V- IMPLOSION EXPERIMENTS

Much has been made of the difference between exploding pusher, large entropy change, low density implosion targets and those described as ablative implosion targets which are designed to achieve high density and high gain. Before discussing some of our experiments which are moving in the direction of the limit of ablative implosion targets, we present examples of the two classes of implosions as calculated by a one-dimensional hydrodynamic code.

Figure 32 presents the distribution of target material as a function of radius, the distribution of the laser energy as a function of time, the radius time history of the target material, and also shows the temperature history of the fuel material. The laser pulse time history is appropriate to Argus exploding pusher experiments where the FWHM of the laser driver pulse was 40 psec. The target radus was 40 μm with a glass wall thickness of a 0.5 μm. As shown in the R vs t history very early in Gaussian laser pulse, the glass shell expands outward and as the laser intensity rises the production of suprathermal electrons, produce energy deposition throughout the glass shell and inward motion of the glass pusher material. 20 psec before the peak of the laser pulse, the strong shock wave produced in the DT gas fuel has already produced a fuel temperature of 80 eV. The glass pusher by this time is significantly decompressed. Electrons are preheating both the fuel and the pusher near the peak of the laser pulse and the temperature has risen to almost 0.5 keV. The shock continues to propagate to the center of the fuel region, reflects at the origin and at the time of stagnation of the

glass pusher and DT fuel region, the temperature has risen to 8.0 keV. Typcal Argus targets had initial fuel densities of 2 mg/cm^3. The compression illustrated in this figure is ~120 leading to a final fuel density of ~1x liquid density of DT.

The reader is now invited to compare Figure 32 to Figure 33, a tutorial example of an ablative driven implosion which achieves ignition temperatures of 7.0 keV and final fuel densities of several thousand times that of liquid DT. The target structure as a function of radius is shown in the left portion of the figure. Low Z Be is used as the high efficiency ablator material to provide the rocket impulse to efficiently drive the fuel to high density. Glass and lead glass are used as a graded density pusher material to provide protection from the suprathermal electrons for both the inner lead glass pusher and the frozen DT fuel. In addition, the graded density distribution reduces the tendency for the growth of the Rayleigh-Taylor instability in the acceleration process of the pusher and the fuel.

The reader should also note the difference in the spatial scale and temporal scale associated with this ablative implosion as compared to that previously presented in the exploding pusher driven implosion. The major differences are that in the previous figure we showed a laser pulse FWHM of 40 psec whereas this target is driven by a laser pulse which extends over 11 ns and the inner fuel radius has increased from 40 μm to 600 μm. Both the shaping of the laser pulse illustrated in the figure and the target structure are used to provide the pressure time history on the fuel and the low level of

preheat of the fuel, both of which allow the fuel to achieve the high density condition necessary for high gain fusion micro-explosions. The temperatures listed in the figure refer to those at the inner edge of the fuel during the implosion process. It is important to note that during the early time history, the fuel has only achieved a temperature of 8.0 eV. The temperature during the later stages of the implosion then rises rapidly during the last 1 ns from 8.0 eV up to in excess of the ignition temperature to 7.0 keV. The conditions achieved in this ablative driven low entropy change implosion would certainly have led to the required conditions for efficient burn of the DT fuel.

We will now turn our attention to experimental and calculational results achieved during the summer of 1979. As illustrated in Figure 34, the early Shiva experiments utilized the exploding pusher concept where the target initial fuel density was 2 mg/cm^3 with glass pusher thicknesses of 1 μm and target diameters of ~300 μm. The laser was operated at 20-30 TW with pulse lengths of 100 psec. In these experiments, the final fuel conditions achieved were 4-8 keV and ~0.1 g/cm^3. The neutron yields were in the range of 10^9 to 10^{10}.

The intermediate density or so called 10x liquid fuel density targets investigated during the summer of 1979 were typically 140 μm inside diameter glass pushers with a wall thickness of 5 μm. The ablator material was $CF_{1.3}$ (Teflon) 15-50 μm thick. These targets were irradiated with 20 TW, 200 psec pulses and achieved ion temperatures of 0.5 - 1.0 keV.[38,39] As indicated by their designation of 10x targets, they typically achieved final fuel densities of 2 g/cm^3 with neutron yields in the range of 10^7 to

10^9. Their pusher areal densities, $\rho\Delta R$, were in the range of 1-2 x 10^{-2} g/cm^2. These targets operated in a transitional region between our classical exploding pusher targets and an ablative driven nearly isentropic compression target.

Figure 35 presents the calculated x-ray spectrum and the experimental data showing the suprathermal portion of the x-ray spectrum. The comparison of the calculation and experiment shows a disagreement of a factor of 2. However, as previously noted in Section IV on the plasma interaction experiments, we have seen a significant variation of the angular distribution of high energy x-rays. The LASNEX calculations do not produce an angular variation of the high energy x-rays and, thus, the differences between the calculations and experiments may be associated with the observed angular distribution. As indicated, we believe that the 10x experiments are not truly ablative driven implosions, but rather represent an intermediate position between exploding pushers and ablative driven implosions.

Figure 36 shows the radius time history as calculated with the LASNEX computer code for the Teflon ablator, the glass pusher and the DT fuel. Early in the laser pulse, several hundred psec before the peak of the laser pulse, the calculations show that the Teflon material is being ablated and that there is a shock propagating through the glass pusher material. However, by the time 100 psec before the peak of the 200 psec FWHM laser pulse, we see that the pusher material is beginning to decompress and that the shock has propagated through the pusher material and is now propagating through the DT fuel. From this time on the glass pusher material continues to decompress until several hundred psec after the peak of the laser pulse at which point

the fuel and the inward motion of the glass pusher stagnate and the outward expansion of pusher and fuel material begins. The major difference besides the final fuel conditions for these experiments and calculations of 10x targets from the Janus, Argus and Shiva exploding pusher targets is in the strength of the initial shock wave driven into the fuel by the inner boundary motion of the glass pusher material and the temperature rise produced by the preheat deposition in the DT fuel.

Figure 37 shows the pressure density history of the fuel for typical exploding pusher targets, our 10x target, targets designed to achieve 100x liquid density and the limiting isentrope which is produced by the Fermi degenerate state of DT.

One of the most complex issues in the diagnostics of high density laser fusion is the determination of the fuel density. We devote a significant fraction of our on-line diagnostic and our Diagnostic Development program to the determination of this quantity. For low final fuel densities, ≤ 0.2 g/cm^{-3}, we have utilized spatial imaging of the α particles produced in the DT reaction[61] and Stark broadening of Ne lines as density diagnostics.[62] For our 10x density targets, we have utilized spatial imaging of the x-rays from the fuel and the pusher, spatial imaging of a seed material in the fuel and neutron activation (rad chem) of the pusher material in conjunction with simple or LASNEX modeling to determine the final fuel conditions.

Table II summarizes the results from a number of our 10x target experiments. Typical incident laser energies varied from 2-4 kJ. The number of DT neutrons produced ranged from 1.5×10^7 to 7×10^8. The rad chem

pusher $\rho\Delta R$ measurements range from 5×10^{-3} g/cm^2 to 6.3×10^{-3} g/cm^2. The simple model interpretation of the experiments[24] presented in Table II would lead to an interpretation of the fuel density of between 4 and 6x liquid density. The LASNEX simulation of these experiments leads to an interpretation of between 6 and 20x liquid density. The large difference here is associated with the question of the diagnostic measurement determining the density at peak burn and the LASNEX calculation predicting that peak compression of the fuel occurs after the peak burn. This mistiming of the peak compression and the peak temperature is easily achieved for these very low fuel temperatures of 0.5-1.0 keV. Mixing of the fuel and the pusher and thermal conduction losses to the cold pusher can easily quench the very inefficient burn of the fuel at these low temperatures.

On four of the experiments presented in Table II, the spatial extent of the seed argon line emission from the fuel was obtained in one spatial direction. This data has been interpreted both assuming a spherical distribution of the argon and fuel and a 2:1 ellipsoidal distribution of the argon and fuel. As shown in the table, this leads to a variation in the interpretation of the density of from 1 to 23x liquid density. Since the errors in the spatial extent of the fuel enter as the cube in determining the final fuel density, the very large uncertainty associated with this data interpretation are not surprising. However, it is gratifying that the interpretation of the data does support the radiochemistry and LASNEX interpretation of the experiments as having achieved 10x liquid density. It should further be noted that the interpretation of the spatial extent of the argon line emission also

suffers from the problem of the mistiming of the peak temperature in the fuel region with respect to the attainment of the peak density. Of course, this mistiming is inferred from the LASNEX calculations. There is as yet no experimental evidence which confirms or denies the mistiming of these two critical peak conditions.

Figure 38 shows the distribution of density and temperature as a function of radius for the LASNEX one-dimensional calculations of our 10x targets. These calculations show this significant effect of the mistiming in these experiments. They also show that if we believe the LASNEX calculations that the simple model assumption for the interpretation of the radiochemistry diagnostics of isothermal, isobaric conditions in the fuel and the pusher are significantly incorrect. However, as previously shown,[24] large deviations from the isothermal, isobaric approximation do not produce significant differences in the interpretation of the fuel density from the measured effective $\rho\Delta R$ of the pusher.

In Figure 39, we show the LASNEX interpretation of fuel density as a function of the radiochemistry measured effective pusher $\rho\Delta R$ in g/cm^2. The range of measured experimental values are from 4.5 to 7 x 10^{-2} g/cm^2. The LASNEX calculations are presented as a curve for the condition in which the fuel mixes with the pusher at burn time and the case in which there is no mixing of the pusher in the fuel. The lower limit of the experimental measurement and the worst condition of mix of the pusher in the fuel at burn time leads to a minimum fuel density of 5x liquid density

of DT. The most optimistic determination of fuel density would be the upper limit of the experimental measurement interpreted with no mix of the fuel and the pusher leading to a peak fuel density of 30x liquid density of DT. The probable value of the fuel density achieved in these experiments is 10x liquid density of DT.

Another technique which can be used to infer the final density of the fuel is to observe the time integrated continuum emission from the laser imploded target. At low x-ray energies one will primarily view the heating of the pusher and ablator material. As one progresses to higher energies, one expects to see the stagnation of the high Z pusher material against the fuel. For high enough x-ray energy one may expect to see not only emission from the stagnation of the pusher against the fuel, but also the reduced continuum emission due to the fuel region.

In Figure 40, we present the two-dimensional image of the 6.5 keV x-ray emission from one of our 10x targets. The emission from the shell being heated by the laser thermal and suprathermal energy deposition near its initial position are clearly demonstrated. We also observe an intense central region due to the stagnation of the pusher against the fuel. A line out of the intensity distribution across this region clearly demonstrates the reduction of emission by the fuel in the central region. This central region of reduced emission is not circular in the picture, but rather has an oblong character. To use this data to determine compression, we have interpreted the peak of the emission distribution as being the boundary between the fuel and the pusher at peak density. Thus, the spatial distribution of this x-ray emission provides a measure of the

spatial extent of the fuel at peak compression. This data also produces a 10x liquid density for the final fuel compression. The problem of measuring final fuel density will continue to be one of the central topics in fusion micro-explosion experiments, at least until the fusion micro-explosion gain is sufficiently large that this is no longer an issue.

We have utilized a variety of techniques in an attempt to confirm our primary approach to density measurements which is that of nuclear activation of materials in the target. For our 10x liquid density experiments, we are confident that we have sufficient verification by three separate techniques so that we have confidence in the measurements at higher densities. We have also utilized these techniques for our exploding pusher or 1x liquid density targets and in addition, we have utilized imaging of the reaction products to confirm the other diagnostic techniques. Thus, as is shown in Figure 41 where we plot the fuel density measured in the experiments as a function of the neutron yield for a wide class of targets, we have significant confidence that these measurements are substantially accurate. The data plotted in this figure are for Shiva experiments and they illustrate that in our present target experiments we have had to trade final fuel density off against neutron yield, or another way of presenting the same result would be to represent neutron yield as final fuel temperature.

As indicated in the introduction of this paper, with a small amount of laser energy we are able to invest this energy to achieve high fuel temperature and thus, neutron yield, or high density and thus, much lower neutron yield and lower fuel temperatures. Advances in target fabrication and in the performance capability of the Shiva laser are expected to allow us to demonstrate densities as high as 1,000x liquid density with Shiva laser system.

SECTION VI - SUMMARY

In 1979 and 1980, significant short wavelength, i.e., $\leq 0.5\ \mu m$, laser target irradiation facilities have and will become available for laser plasma interaction and implosion experiments. Data already obtained from these facilities confirm the promise of improved laser plasma interaction conditions and implosion target performance. The theory predicted scaling of the suprathermal electron temperature with $I\lambda^2$ may actually be conservative due to the significantly increased inverse bremstrahlung absorption of the laser energy by the targets at shorter wavelengths, thus, preventing conversion of the incident laser energy to suprathermal electrons at the critical density by resonance absorption. The demonstration of scientific breakeven and scientific feasibility in inertial fusion requires that we have a facility with sufficient energy and power delivery capability to perform these demonstration experiments.

The Nova Nd glass laser design at LLL shows that a facility of 100 kJ and 100 TW can easily be achieved in the next several years. The full development of the Nova facility can provide 400 kJ in a 3 ns pulse length. Fusion reactors will require the development of an efficient short wavelength or ion beam driver. However, the technology of the Nd glass laser has been developed to the point that a MJ class Nd glass facility could easily be developed in the 1985-87 time frame to prove the performance requirements of inertial confinement fusion targets.

Laser fusion target fabrication developments have also progressed to allow both fusion target performance development, and to accommodate diagnostic

measurement requirements. In conjunction with this, we have been able to develop critical and definitive new diagnostic instruments which utilize these fabrication developments. We have also been successful in extending our capability to measure the spatial, temporal and spectral behavior of the fusion targets.

One of the most important developments of the last several years has been the understanding of the scaling of the laser plasma conditions to the scales required for reactor targets. This understanding of the scaling properties has led to a significant amelioration of the deleterious laser plasma effects observed over the last several years with exploding pusher targets.

Finally, we have made a significant effort to begin our exploration of the high density, low entropy change targets which are required for reactor conditions. Our intermediate or 10x targets, both calculations and experiments, have been discussed in Section V of this paper. We have also produced experimental data and calculations on targets which have achieved 100x liquid DT density.

ACKNOWLEDGMENTS

This invited paper at the 1980 joint CLEOS/ICF Conference was requested by the Program Committee to be a progress report on the Laser Fusion Program at the Lawrence Livermore Laboratory. I have chosen to restrict myself to developments in target facilities, diagnostics, interaction experiments and implosion experiments. The impressive developments in reactor driver requirements and developments and reactor system studies are well represented by other papers at this conference.

The material presented in this paper has been developed and produced by the Fusion Laser Program Element under the leadership of J. F. Holzrichter, the Targets Program Element under the leadership of J. H. Nuckolls and the Fusion Experiments Program Element directed by the author.

The Fusion Laser Program Element has been responsible for the development of the facilities and since June 1979 when the systems operations were transferred from Fusion Experiments to Fusion Lasers, they have also been responsible for the operation and maintenance of the Shiva and Argus target irradiation facilities.

The Target Design and Target Fabrication Program Elements have continued to work closely and in conjunction with the Fusion Experiments Program Element to define, calculate, fabricate, execute, diagnose and analyze the laser fusion target experiments.

In the Fusion Experiments Program Element, the Experiments Group is headed by K. R. Manes, the Laser Fusion Diagnostics Group is headed by V. W. Slivinsky, the Diagnostics Developments Group is lead by D. T. Attwood and the Data Management and Analysis Group is unofficially directed by J. Greenwood.

The material presented herein has come from all three of the above mentioned program elements, however, those who have made direct contributions are (alphabetically): J. Attwood, J. Auerbach, D. Banner, M. Campbell, N. Ceglio, L. Coleman, J. Glaze, J. Hunt, R. Kauffman, W. Kruer, S. Lane, J. Larsen, P. Lee, C. Lindl, K. Manes, D. Matthews, W. Mead, J. Nuckolls, D. Phillion, R. Price, F. Rienecker, M. Rosen, V. Rupert, G. Tirsell, C. Wang and J. Zickuhr.

Jaci Nissen provided the rapid, accurate translation from dictation and the typing of this document, and Linda Kruger worked with those named above to produce the final document.

REFERENCES

1. G Dahlbacka and J. Nuckolls, "Laser Driven Isothermal Implosions", Lawrence Livermore Laboratory, Livermore CA, UCRL-75885 (Oct. 28, 1974).

2. H. G. Ahlstrom, "Laser Fusion Implosion and Plasma Interaction Experiments", Lawrence Livermore Laboratory, Livermore, CA, UCRL-79819 (August 1977).

3. E. K. Storm, H. G. Ahlstrom, M. J. Boyle, D. E. Campbell, L. W. Coleman, S. S. Glaros, H. N. Kornblum, R. A. Lerche, D. R. MacQuigg, D. W. Phillion, F. Rainier, F. Rienecker, V. C. Rupert, V. W. Slivinsky, D. R. Speck, C. D. Swift and K. G. Tirsell, "Laser Fusion Experiments at 4 TW", Phys. Rev. Lett. 40, 24 (1978).

4. J. Nuckolls, L. Wood, A. Theissen and G. Zimmerman, "Laser Compression of Matter to Super-High Densities: Thermonuclear (CTR) Applications", Nature (Lond.), 239, pp. 139-142 (Sept. 1972).

5. J. D. Lindl, "Low-Aspect Ratio Double Shells for High Density and High Gain", Laser Program Annual Report-1977, Lawrence Livermore Laboratory, Livermore, CA, UCRL-50021-77, pp. 4-12 to 4-15 (July 1978).

6. ibid., J. H. Nuckolls, R. O. Bangerter, J. D. Lindl, W. C. Mead and Y. L. Pan, "High-Performance Inertial Confinement Fusion Targets", pp. 4-15 to 4-19.

7. ibid., C. D. Hendricks, "Target Fabrication Overview", pp. 5-1 to 5-5.

8. J. J. Ewing, R. A. Haas, J. C. Swingle, E. V. George and W. F. Krupke, "Optical Pulse Compressor Systems for Laser Fusion", IEEE J. Quantum Electron., Qe-15, 5, pp. 368-379 (May 1979).

9. op. cit., No. 5, Section 7.

10. Section 8, Laser Program Annual Report-1978, Lawrence Livermore Laboratory, Livermore, CA, UCRL-50021-78 (March 1979).

11. J. Hunt, J. Swain and B. Johnson, "Argus 2ω/3ω Modifications", Section 2.2.2, Laser Program Annual Report-1979, Lawrence Livermore Laboratory, Livermore, CA, UCRL-50021-79.

12. A. G. M. Maaswinkel, K. Eidmann and R. Sigel, "Comparative Reflectance Measurements on Laser Produced Plasmas at 1.06 and 0.53 μm", Phys. Rev. Lett., 42, 24, pp. 1625-1628 (June 1979).

13. F. Amiranoff, R. Benattar, R. Fabbro, E. Fabre, C. Garban, M. Weinfeld, "Effect of Wavelengths and Pulse Durations on Absorption and Heating in Laser Irradiated Target Experiments", Bull. Am. Phys. Soc., 24, 8, p. 1054 (Oct. 1979).

14. M. H. Key, et.al., "Review of Recent Work at the SRC Central Laser Facility at the Rutherford Laboratory, Abingdon", XIII European Conference on Laser Interaction with Matter, Leipzig, GDR (Dec. 1979).

15. op. cit., No. 11, E. M. Campbell, C. E. Max, D. W. Phillion, P. H. Y. Lee and M. Rosen, "Disk Experiments: 2ω Absorption, 2 ns Absorption", Section 6.3.

16. K. R. Manes, H. G. Ahlstrom, R. A. Haas and J. F. Holzrichter, J. Opt. Soc. Am., 67, 6, pp. 717-726 (1977).

17. op. cit., No. 10, T. J. Gilmartin, R. O. Godwin, J. F. Holzrichter and W. W. Simmons, "Nova Development", Section 2.4.

18. J. A. Glaze, W. W. Simmons and J. B. Trembolme, "Update of Nova Chain Design and Performance", Nova Memorandum 79-640 (Jan. 1980).

19. op. cit., No. 11, L. Smith and M. Summers, "Large Aperture Frequency Conversion", Section 2.4.8.

20. op. cit., No. 10, W. L. Kruer, "Raman Backscatter in High Temperature, Inhomogeneous Plasmas", pp. 3-42 to 3-46.

21. op. cit., No. 11, D. W. Phillion, "Raman Spectrometer", Section 5.15.

22. ibid., R. Kauffman, "Development of a Time Resolved, Broad-Band Sub-Kilovolt X-ray Spectrometer for Absolute Flux Measurements", Section 5.5.

23. K. G. Tirsell, R. A. Heinle, H. N. Kornblum and V. W. Slivinsky, "Time Resolved, X-ray Measurements Below 700 eV Using Filtered, X-ray Diodes with and without Mirror Cut-Off", Bull. of Am. Phys. Soc., 24, 8, p. 1099 (Oct. 1979).

24. H. G. Ahlstrom, "Progress of Laser Fusion at Lawence Livermore Laboratory", to be published in Journal de Physique.

25. op. cit., No. 10, D. T. Attwood and N. M. Ceglio, "X-ray Probing Diagnostics for High Density Implosion Experiments", pp. 6-38 to 6-40.

26. M. J. Boyle and H. G. Ahlstrom, "Imaging Characteristics of an Axisymmetric, Grazing Incident X-ray Microscope Designed for Laser Fusion Research", Rev. Sci. Instrum., 49, 746 (1978.)

27. op. cit., No. 10, R. H. Price and M. J. Boyle, "Wolter Axisymmetric X-ray Microscope Development", pp. 6-23 to 6-26.

28. op. cit., No. 11, D. W. Phillion, "Shiva Optical Preheat Detector", Section 5.15.

29. E. M. Campbell, W. M. Ploeger, P. H. Lee and S. M. Lane, "Exploding-Pusher-Tamper $\rho\Delta R$ Measurement by Neutron Activation", Lawrence Livermore Laboratory, Livermore, CA, UCRL-83096 (Oct. 1979).

30. E. M. Campbell, H. G. Hicks, W. C. Mead, L. W. Coleman, C. W. Hatcher, J. H. Dellis, M. J. Boyle, J. T. Larsen and S. M. Lane, "Collection-Fraction Determination Utilizing a Radioactive Tracer", Lawrence Livermore Laboratory, UCRL-83072 (July 1979), to be published in J. Appl. Phys. (April 1980).

31. op. cit., No. 10, E. M. Campbell, "Neutron Activation Diagnostics for High Density Targets", pp. 6-45 to 6-52.

32. E. M. Campbell, S. M. Lane, Y. L. Pan, J. T. Larsen, R. J. Wahl and R. H. Price, "Determination of Fuel ρR of ICF Tartets by Neutron Activation", Lawrence Livermore Laboratory, Livermore, CA, UCRL-83073, to be published in J. Appl. Phys. (April 1980).

33. op. cit., No. 11, S. Lane, "Implosion Measurements with Radiochemistry Techniques", Section 5.11.

34. ibid., D. W. Phillion and K. Estabrook, "Stimulated Raman Scattering Studies at Argus", Section 6.5.

35. op. cit., No. 23, C. L. Wang, H. N. Kornblum and V. W. Slivinsky, "Suprathermal X-ray Angular Distribution from Laser-Produced Plasmas", p. 1106.

36. G. McClellan, P. H. Y. Lee and G. Caporaso, "Z Dependence of Laser Intensity Threshold for Inhibited Electron Thermal Conduction", Lawrence Livermore Laboratory, Livermore, CA, UCRL-83044, Rev. 2, submitted to Phys. Rev. Lett.

37. op. cit., No. 23, J. M. Auerbach, K. R. Manes, D. L. Matthews, L. N. Koppel, S. M. Lane, E. M. Campbell, N. M. Ceglio, D. W. Phillion, P. H. Y. Lee, V. C. Rupert, D. L. Banner, C. D. Swift, C. W. Hatcher and W. C. Mead, "Experiments with Polymer Coated Microspheres Irradiated by the Shiva Laser System", p. 1011.

38. J. M. Auerbach, W. C. Mead, E. M. Campbell, D. L. Matthews, D. S. Bailey, N. M. Ceglio, C. W. Hatcher, L. N. Koppel, S. M. Lane, P. H. Y. Lee, K. R. Manes, S. McClellan, D. W. Phillion, R. L. Price, V. C. Rupert, V. W. Slivinsky and C. D. Swift, "Compression of Polymer Coated Laser Fusion Targets to 10x Liquid DT Density", Lawrence Livermore Laboratory, Livermore, CA, UCRL-83989, submitted to Phys. Rev. Lett.

39. W. C. Mead, C. D. Orth, D. S. Bailey, G. McClellan and K. G. Estabrook, "Analysis of Dense Laser-Driven Implosion for Intermediate Densities", Lawrence Livermore Laboratory, Livermore, CA, UCRL-83163 (Oct. 1979).

40. op. cit., No. 10, Section 2.2 Shiva Accomplishments and Section 2.3 Shiva System Development.

41. op. cit., No. 11, J. M. Auerbach, "Target Alignment Codes: ALIGN, GEOBM, LITAR, PLANAR", Section 6.11.5.

42. op. cit., No. 10, K. R. Manes and F. D. Feiock, "Laser Irradiation on Target (LITAR) Code", pp. 6-66 to 6-67.

43. W. Lee Smith and T. F. Deaton, "Array Technology for Large Aperture Harmonic Generation", Paper Th F7, Topical Meeting on Inertial Confinement Fusion, San Diego (Feb. 1980).

44. J. Foster, "Ad Hoc Experts Group on Fusion Report" (July 1979).

45. op. cit., No. 10, W. E. Martin, "Progress in Rectangular Disk Amplifiers, pp. 7-4 to 7-8.

46. J. T. Hunt, et al., "Improved Performance of Fusion Lasers Using the Imaging Properties of Multiple Spatial Filters", Applied Optics, 16, 4, pp. 779-782 (April 1977).

47. op. cit., No. 10, D. Campbell, W. Laird and T. Schwinn, "Windowless X-ray Detector with 50-psec Response", pp. 6-64 to 6-65.

48. R. L. Kauffman, H. Medecki and E. L. Pierce, "A Pulsed Calibration of the Soft X-ray Streak Camera", Lawrence Livermore Laboratory, Livermore, CA, UCRL-83095 (Nov. 1979).

49. op. cit., No. 23, J. Cheng, J. Noonan and G. Tripp, "CCD/Streak Camera Data Acquisition System", p. 1099.

50. D. T. Attwood, et al., "Space Time Implosion Characteristics of Laser Irradiated Fusion Targets", Phys. Rev. Lett., 38, 6 (Feb. 1977).

51. op. cit., No. 5, D. J. Kuizenga, "Actively Mode-Locked and Q-Switched Oscillator", pp. 2-207 to 2-210.

52. ibid., J. E. Murray, "Regenerative Pulse Compression", pp. 2-210 to 2-219.

53. op. cit., No. 10, N. M. Ceglio, "Fresnel Zone Structures for Advanced X-ray Microscopy", pp. 6-30 to 6-37.

54. op. cit. No. 23, L. N. Koppel, T. W. Barbee and D. T. Attwood, "Synthetic Multi-layer Structures as Medium Bandwidth X-ray Reflectors", pp. 1098-1099.

55. ibid., D. T. Attwood and N. M. Ceglio, "X-ray Probing of Laser Compressed Targets", pp. 1105-1106.

56. op. cit. No. 10, D. W. Phillion, "Optical Preheat Diagnostic", pp. 6-40 to 6-45.

57. op. cit., No. 11, V. W. Slivinsky and M. D. Rosen, Isothermal-Isobaric Implosion Model", Section 6.9.

58. ibid., Meyer and Johnson, "High Atomic Number Coatings", Section 4.3.2.

59. ibid., Morrison, "Glass Sphere Development and Production, Diagnostic Gas Fills", Section 4.2.2.

60. NRL Laser/Plasma Group, NRL Memorandum Report 3890 (Dec. 1978).

61. N. M. Ceglio and L. W. Coleman, "Spatially Resolved Alpha Emission from Laser Fusion Targets", Phys. Rev. Lett., 39, pp. 20-24 (1977).

62. J. M. Auerbach, et al., "Neon Spectral Line Broadening as a Diagnostic for Compressed Laser Fusion Targets", J. Appl. Phys., 50B, pp. 5478-5482 (Aug. 1979).

LASER FUSION -- PROGRESS/PROJECTIONS

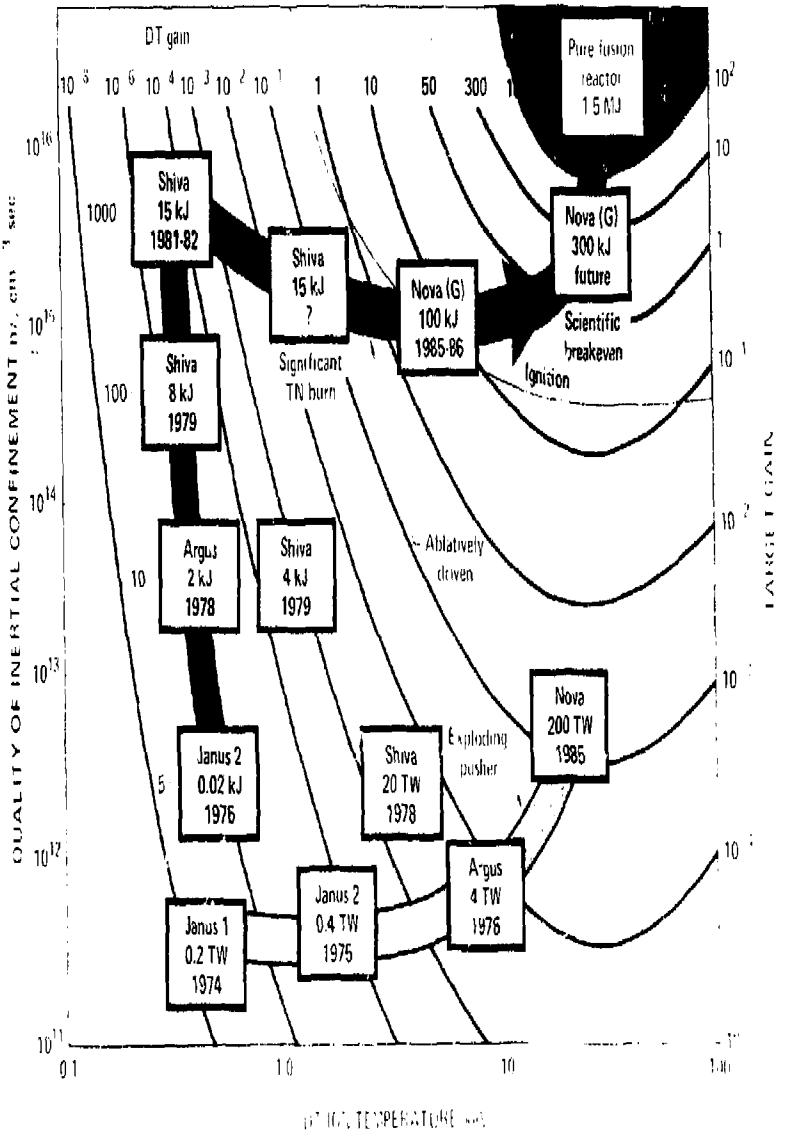

50-90-1279-5190

Figure 1

SHIVA TARGET ILLUMINATION – TANGENTIAL FOCUSSING

Polar plot of beam positions Geometric optics cones' intersection with a 190 μm radius hemisphere

Hemisphere represented by Polar Grid

Radial mesh $\Delta\theta = 10^{\circ}$
Azimuthal mesh $\Delta\varphi = 20^{\circ}$

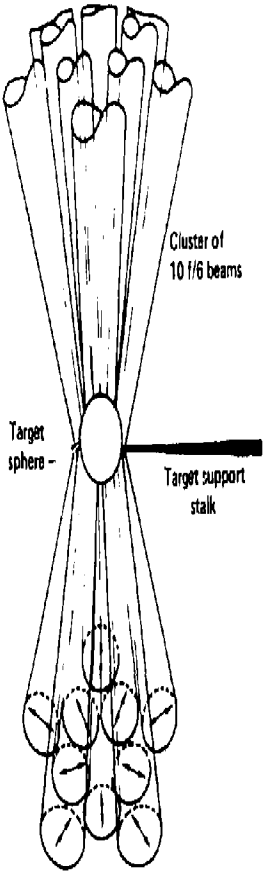

Calculated incident intensity distribution using diffraction theory for a 190 μm dia ball irradiated by 4 kJ/200 psec

White 2×10^{16} W/cm^2
Yellow 1.4×10^{16} W/cm^2
Brown 9.7×10^{15} W/cm^2
Orange 6.4×10^{15} W/cm^2
Red 2.8×10^{15} W/cm^2

02-30-0180-0256

Figure 2

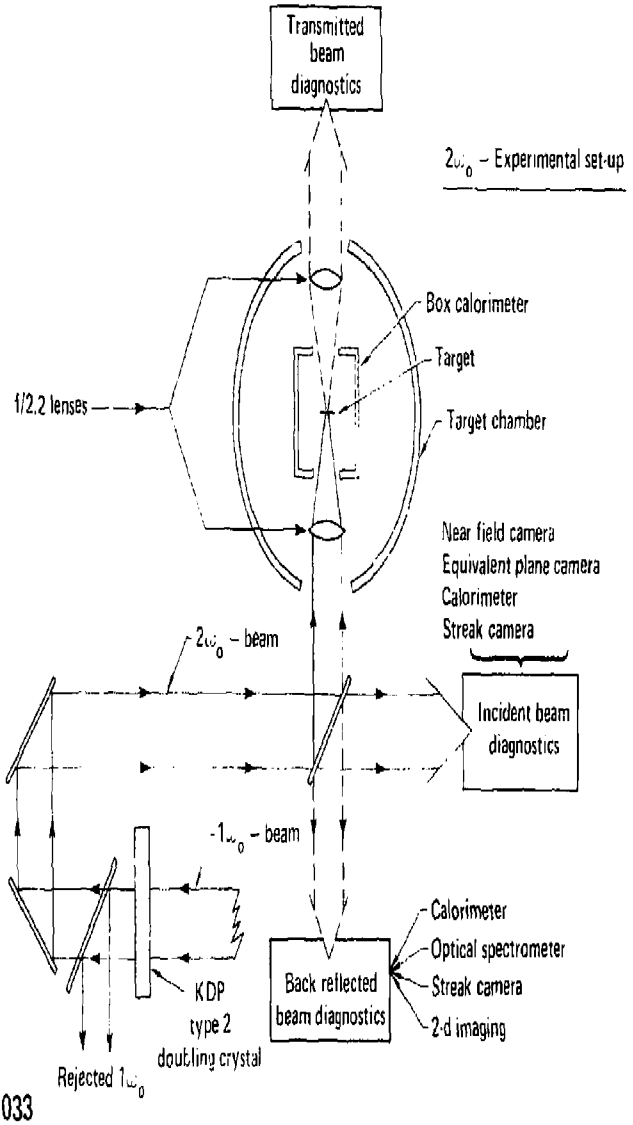
Transmitted beam diagnostics
$2\omega_0$ – Experimental set-up
Box calorimeter
Target
Target chamber
f/2.2 lenses
Near field camera
Equivalent plane camera
Calorimeter
Streak camera
$2\omega_0$ – beam
Incident beam diagnostics
$-1\omega_0$ – beam
Calorimeter
Optical spectrometer
Streak camera
2-d imaging
Back reflected beam diagnostics
KDP type 2 doubling crystal
Rejected $1\omega_0$
20-05-0180-0033

Figure 3

NOVA CHAIN DESIGN

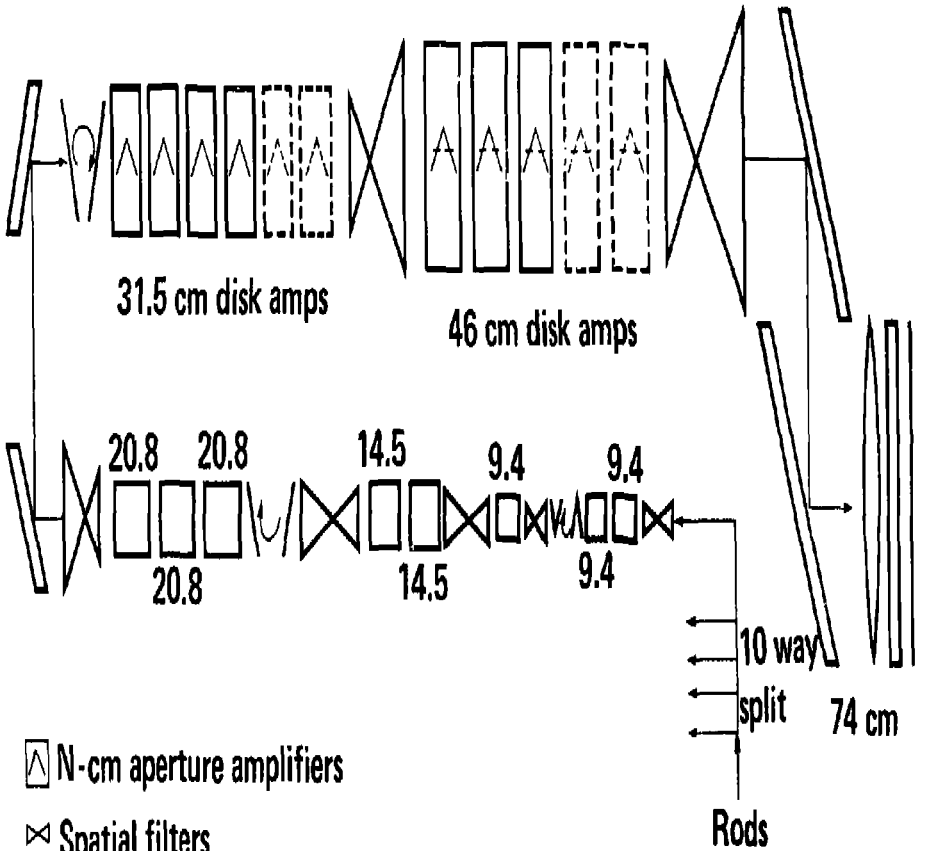

- N-cm aperture amplifiers
- Spatial filters
- Faraday isolators
- Mirrors
- Focus lens, window, debris sheild

Optical schematic showing one (of 10) nova phase I amplifier chains. Following the amplifiers, a final spatial filter expands the beam to 74 cm clear aperture for transport to the (AR coated) target focusing optics. Dashed amplifiers indicate later amplifier additions for higher energy.

02-31-0180-0047

Figure 4

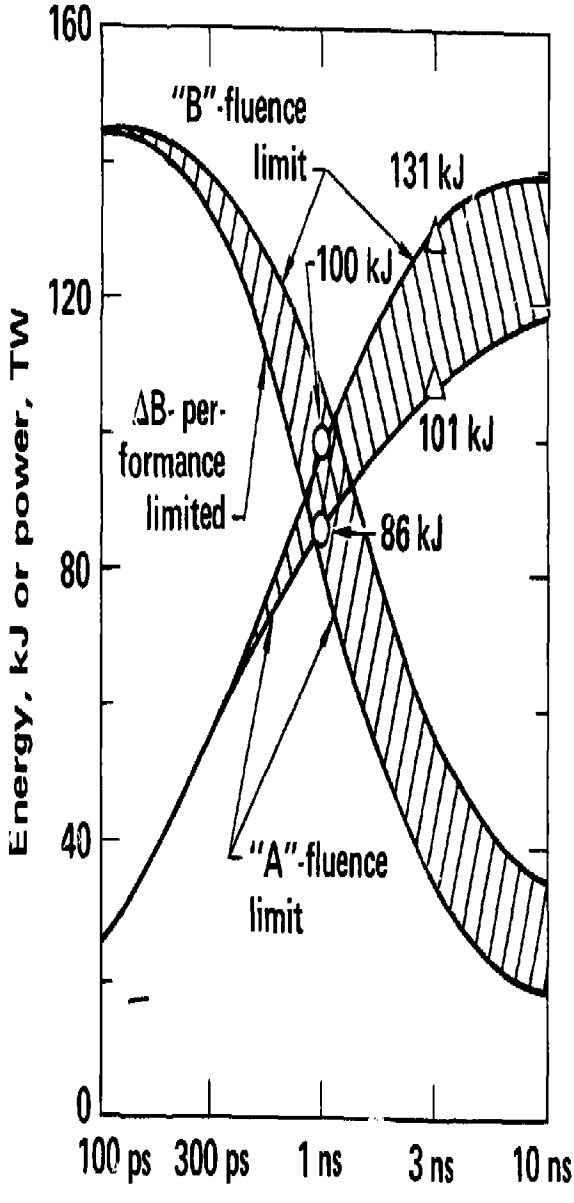

02-31-0180-0045A

Figure 5

NOVA TARGET CHAMBER PHASE 1

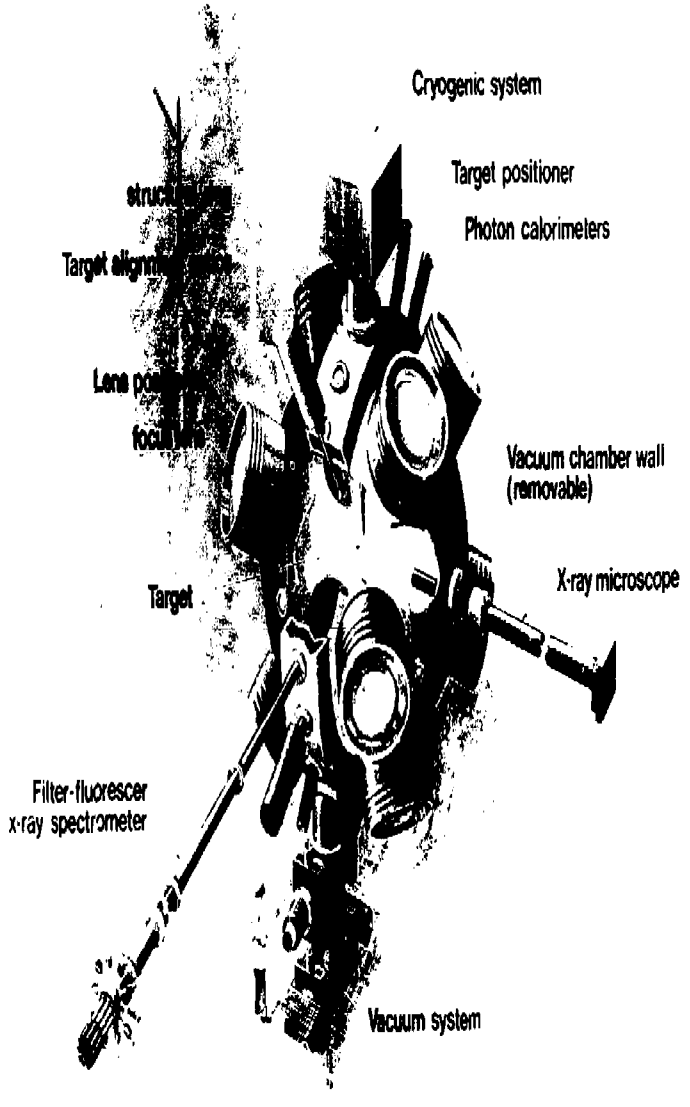

Figure 6

NOVA TARGET ILLUMINATION

Large Cone Angle Allows Nearly Uniform Irradiation

Beam alignment on a 2000 μm dia sphere

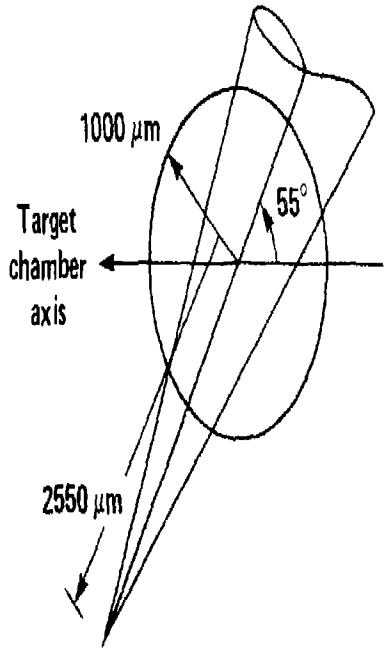

Beam geometry
5 beams/hemisphere
f/3.0 lenses
55° polar angle between lens and chamber axes with 72° azimuthal separation between beams

02-31-0280-0370

Polar plot of right hemisphere

Calculated intensity distribution for shown alignment and 10 TW/beam. Outer radius corresponds to equator.

Color code:

White: 1.2×10^{15} W/cm^2
Yellow: 6×10^{14} W/cm^2
Red: 3×10^{14} W/cm^2
Green: 1.5×10^{14} W/cm^2

Figure 7

LIGHT COLLECTOR FOR A SHIVA DOME PORT AT $\theta = 20^{\circ}$

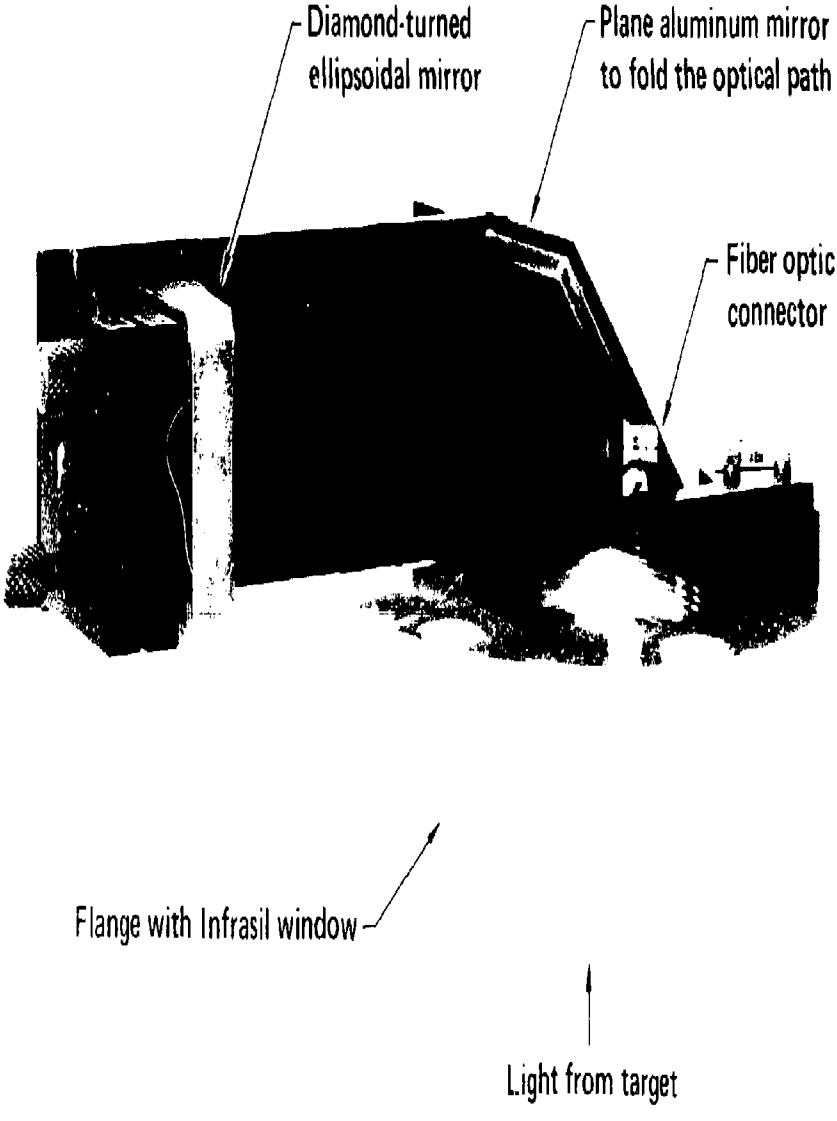

02 30-0280-0409

Figure 8

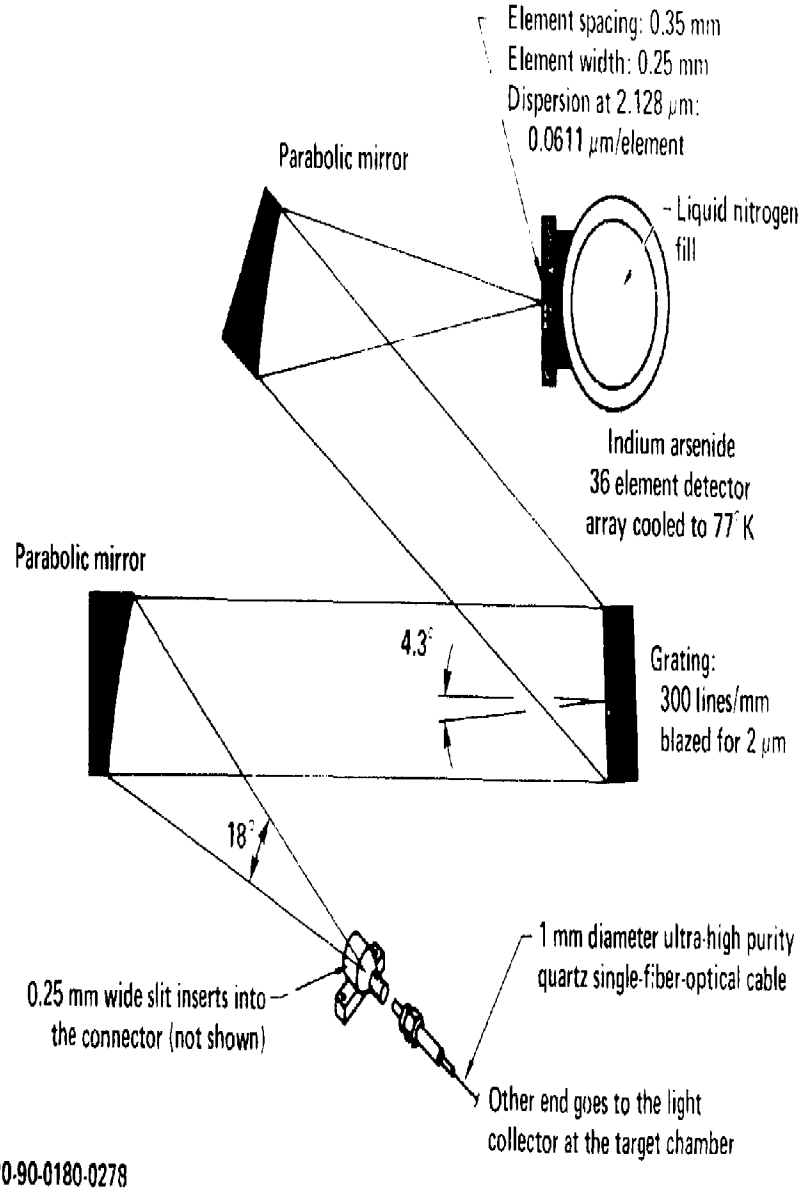
Element spacing: 0.35 mm
Element width: 0.25 mm
Dispersion at 2.128 μm:
0.0611 μm/element
Parabolic mirror
Liquid nitrogen fill
Indium arsenide
36 element detector
array cooled to 77° K
Parabolic mirror
4.3°
Grating:
300 lines/mm
blazed for 2 μm
18°
1 mm diameter ultra-high purity
quartz single-fiber-optical cable
0.25 mm wide slit inserts into
the connector (not shown)
Other end goes to the light
collector at the target chamber
20-90-0180-0278

Figure 9

FIVE CHANNEL MIRROR DANTE ARRANGEMENT

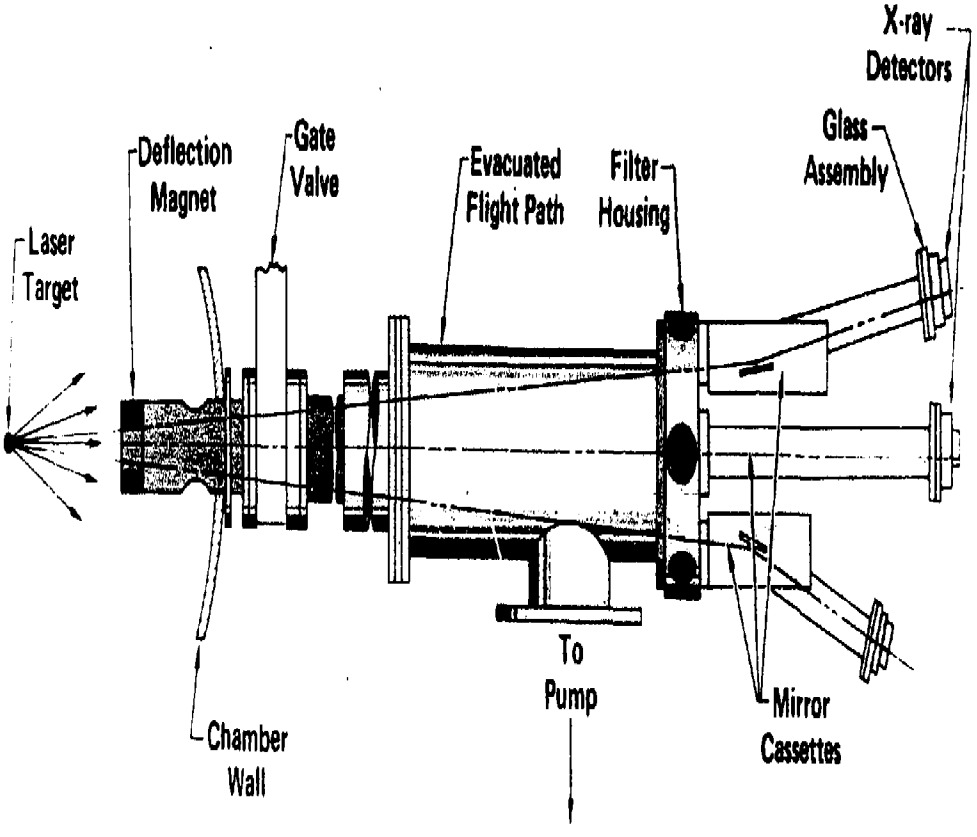

Figure 10

TYPICAL MIRROR "DANTE" CHANNEL

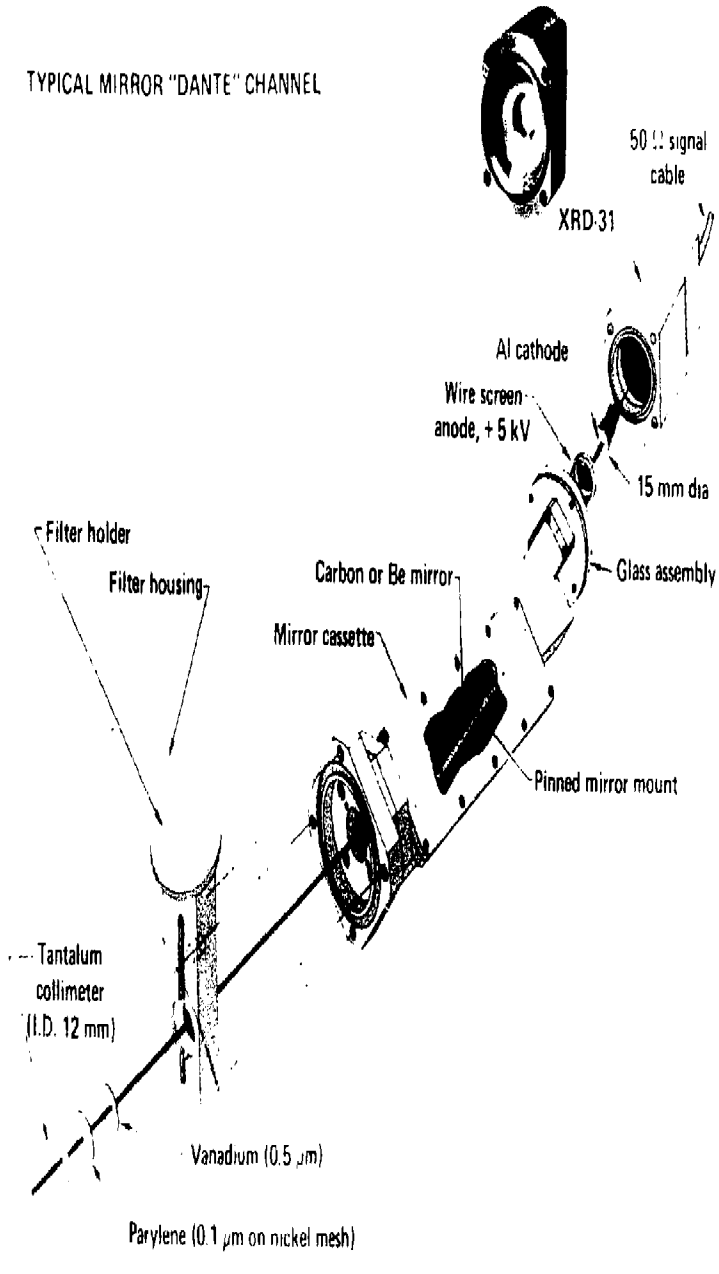

Figure 11

MIRROR DANTE CHANNEL RESPONSES

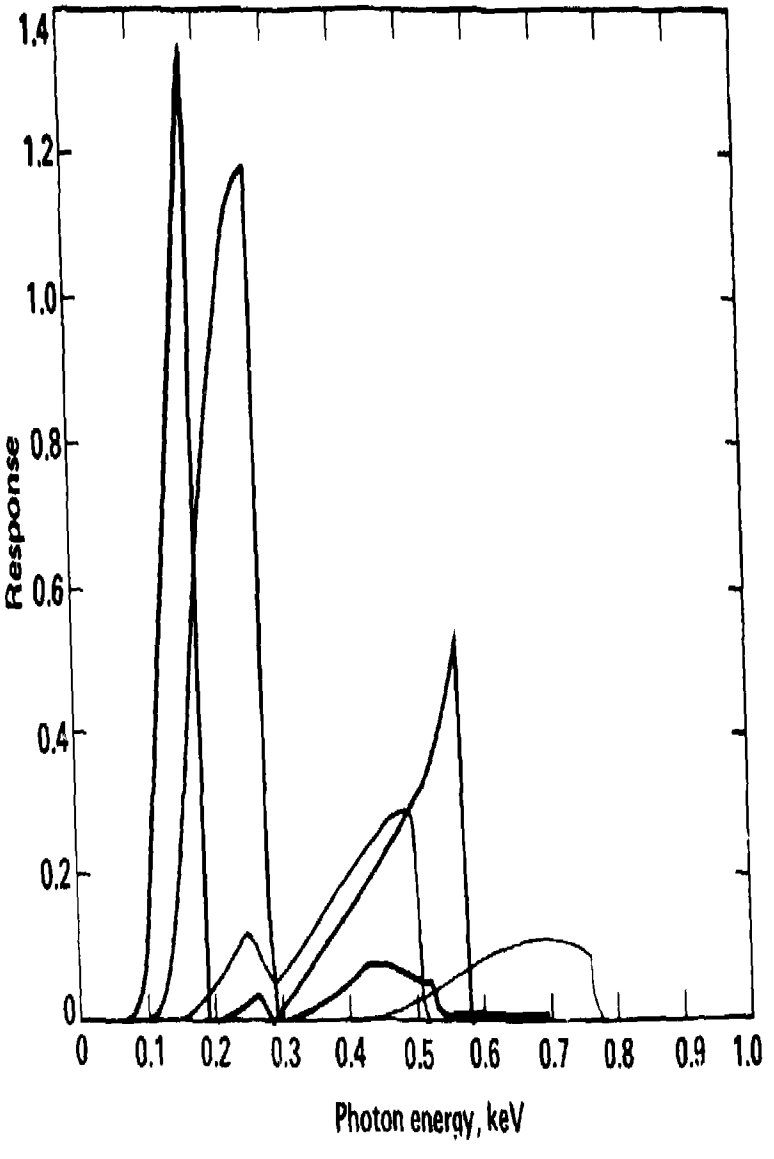

20-90-0180-0241

Figure 12

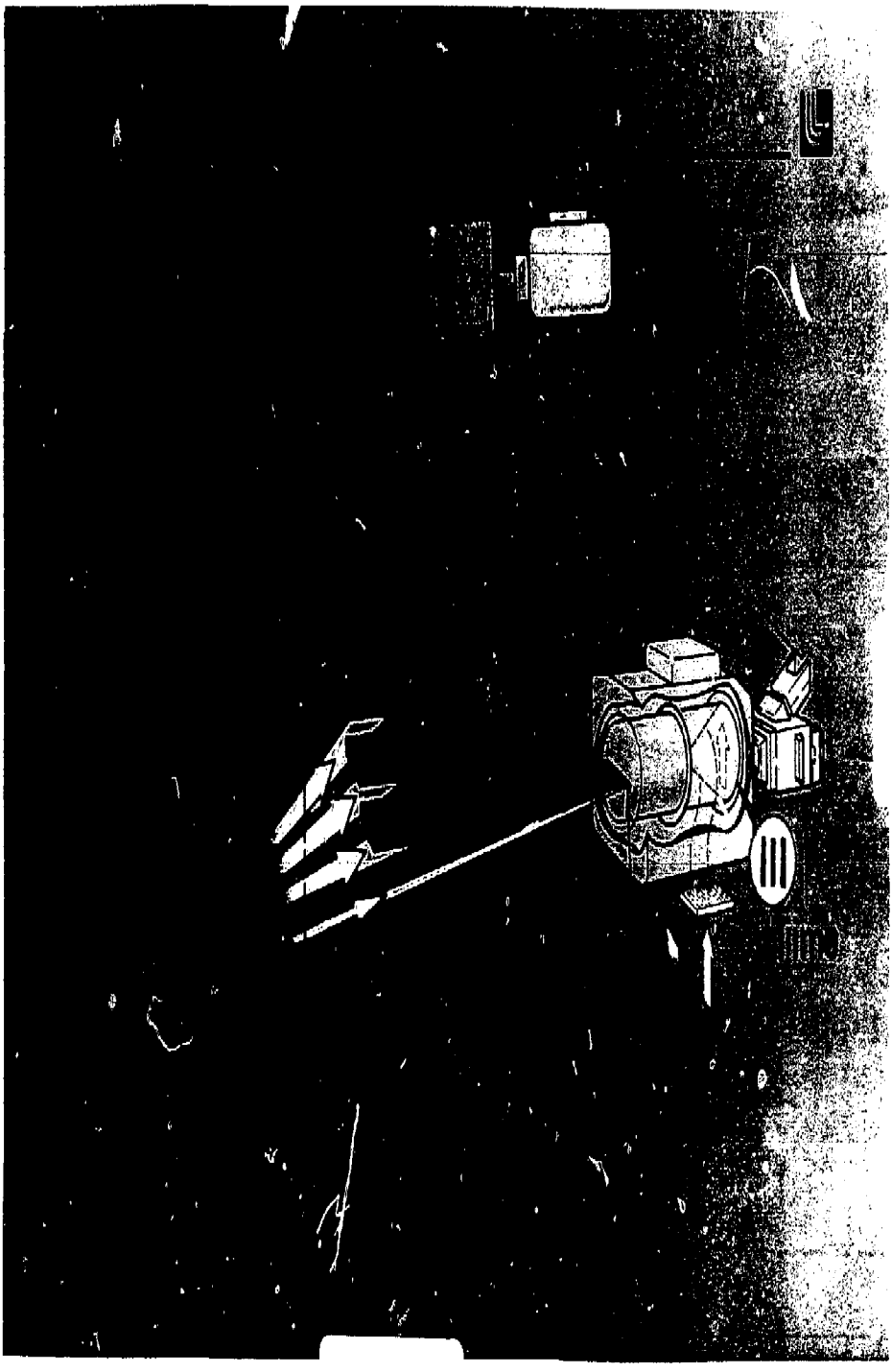

Figure 13

CHANNEL RESPONSES FOR SX-2 ON SHIVA

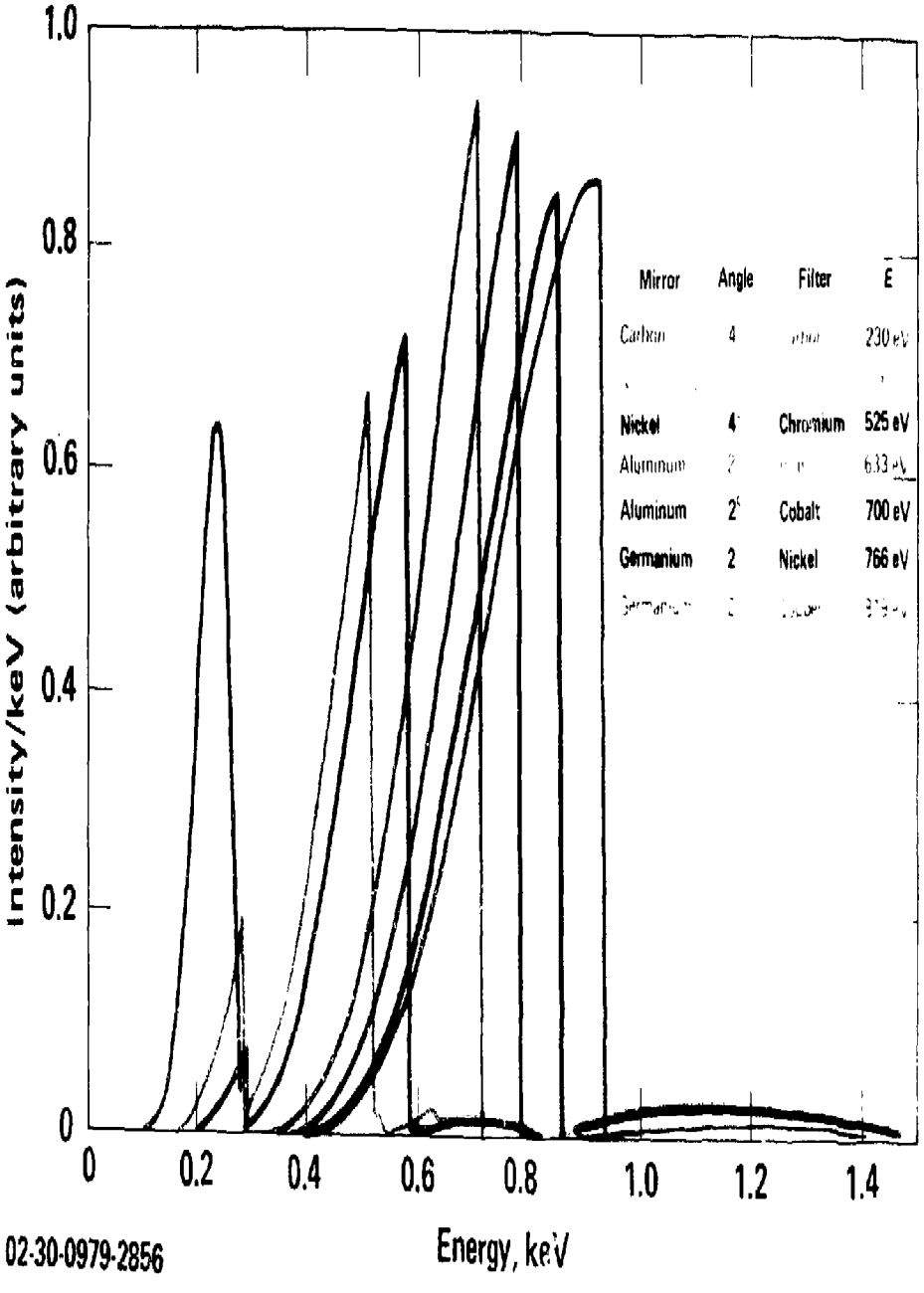

02-30-0979-2856

Figure 14

SHIVA BACK LIGHTING SYSTEM

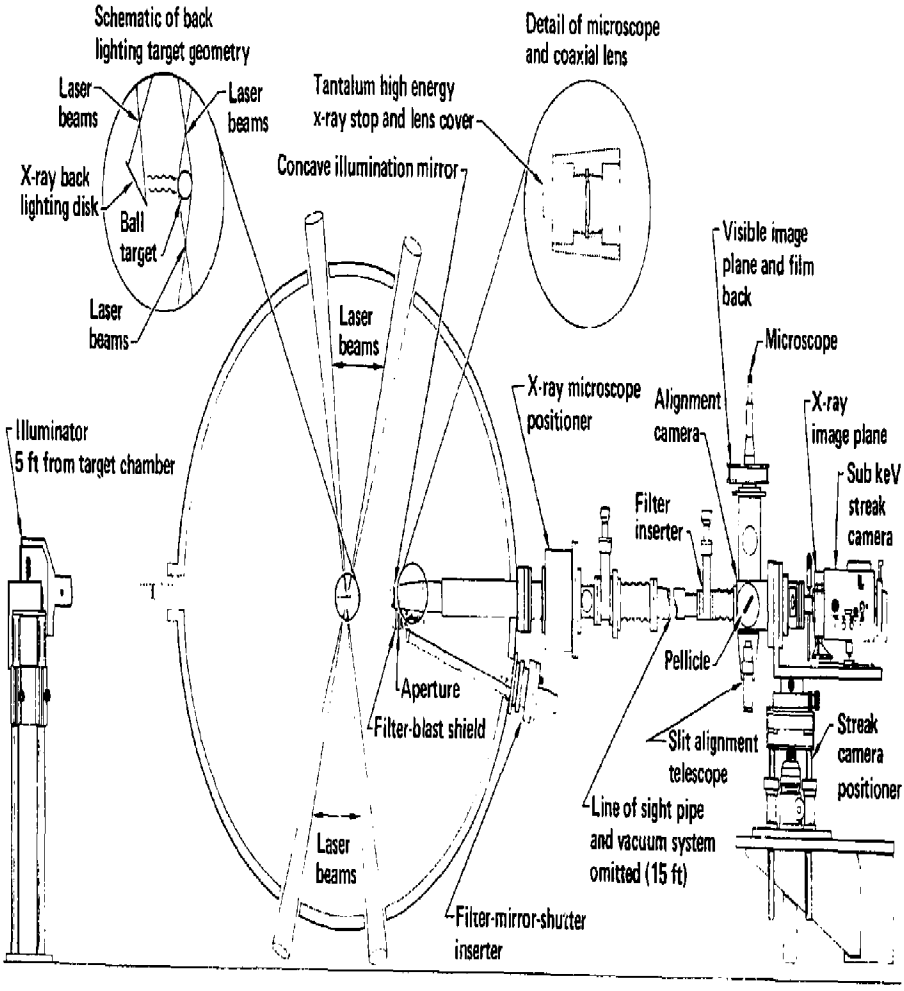

02-30-0280-0391

Figure 15

X-RAY BACKLIGHTING LINE SOURCE DATA

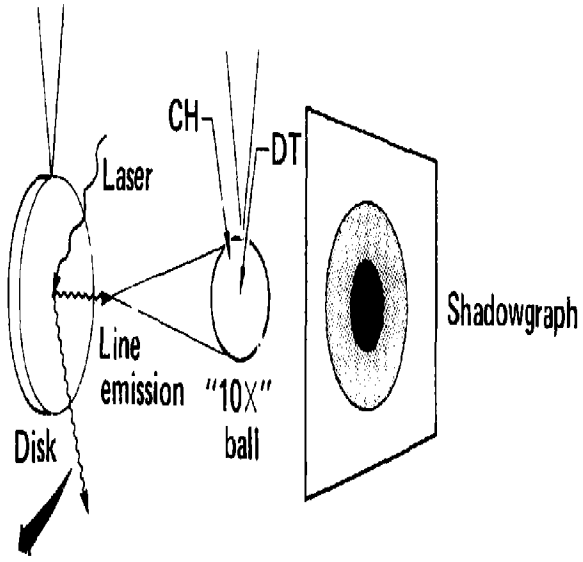

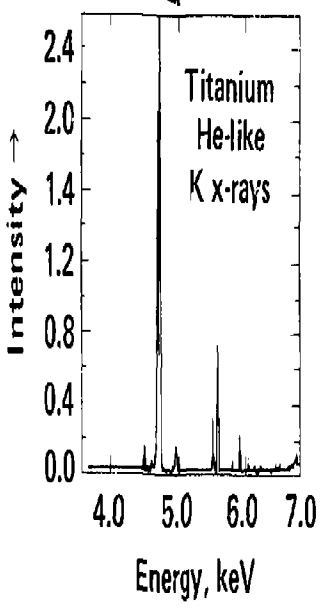

Disk	$E_{h\nu}$ (keV)	I_L (w/cm^2)	τ (ps)	Conversion η (%)
Ti	~4.8	3×10^{15}	600	0.06
Ni	~7.8	3×10^{16}	600	0.08
Zn	~9.0	3×10^{16}	600	0.02

20-50-0280-0337

Figure 16

OPTICAL PYROMETER – TOP VIEW

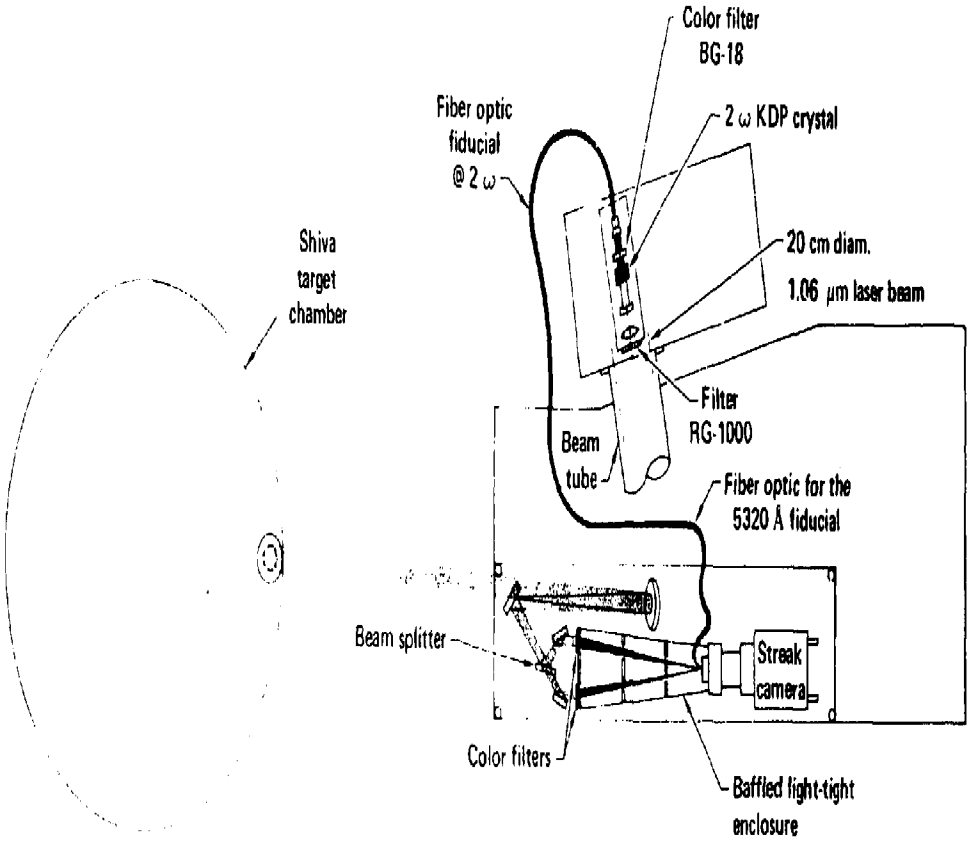

Figure 17A

OPTICAL PYROMETER – PLAN VIEW

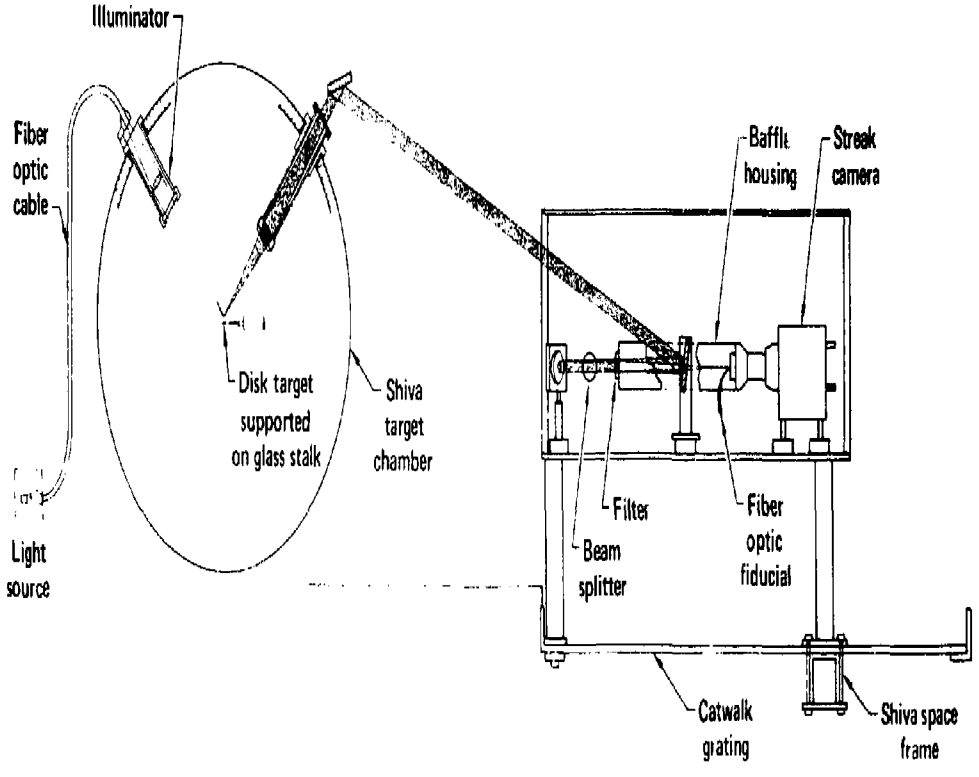

Figure 17B

STUDY OF SUPRATHERMAL e^- PRODUCTION USING K_α X-RAY EMISSION

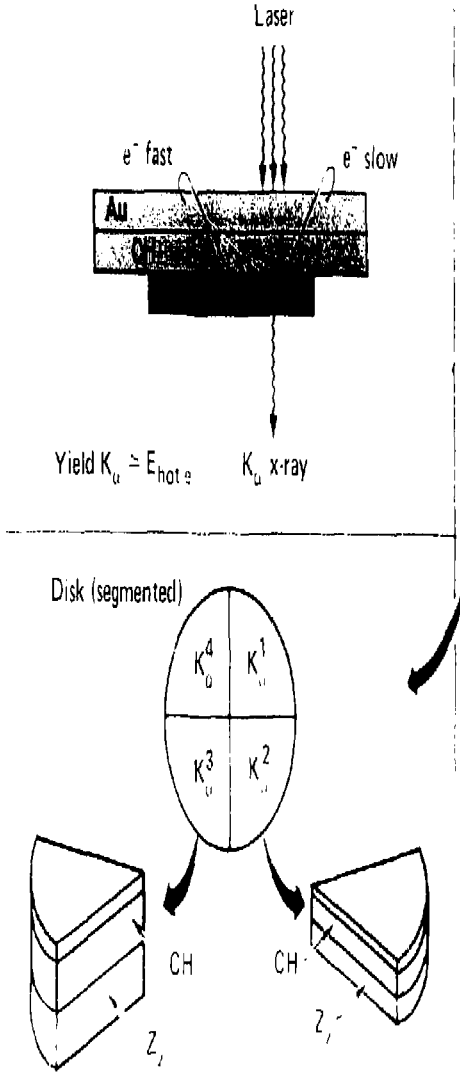

Applications:

- Investigate E_{hot} as function of laser pulse length and intensity
- Study spatial distribution of E_{hot} production by placement of K_α x ray disks at different areas in laser target interaction
- $f_e(E_e)$ determinations by using disks of different CH thickness to sample different portion of e^- spectrum

$$\text{Yield } K_\alpha \propto \int_{E_{min}}^{\infty} E_e \cdot \text{flux}(E_e)\,dE_e$$

CH thickness determines E_{min}

20-50-0280-0345

Figure 19

POSITRON DETECTION SCHEME

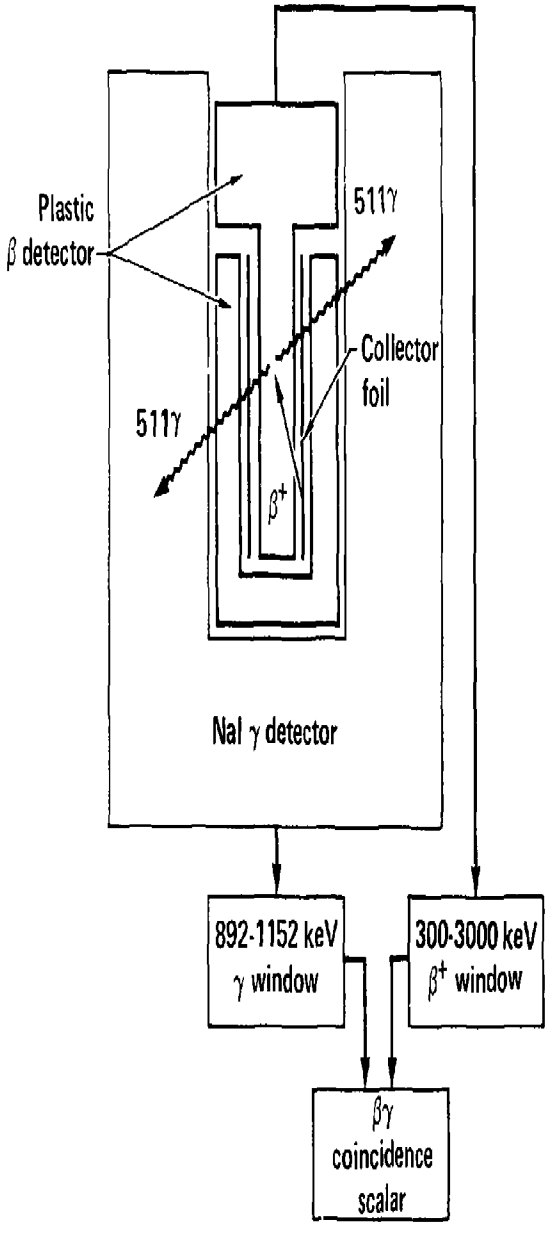

20-01-0280-0343

Figure 19

NEUTRON ACTIVATION
MEASUREMENTS OF PUSHER AND FUEL AREAL DENSITIES

	Si	Cu	Br	
	$^{28}Si(n,p)\ ^{28}Al$	$^{63}Cu(n,2n)\ ^{62}Cu$	$^{79}Br(n,2n)\ ^{78}Br$	Reaction of interest
σ(mb)	250 ± 30	480 ± 20	862 ± 50	Reaction cross-section at 14.1 MeV
f	0.25 ± 0.01	0.6909	0.5034	Fractional abundance of reactant atoms
A(g)	20 ± 1	63.546	–	Average pusher atomic weight
η_D	0.35 ± 0.02	0.54 ± 0.02	0.51 ± 0.02	Radiation detection efficiency
η_C	0.55 ± 0.01	0.55 ± 0.01	0.55 ± 0.01	Debris collection efficiency
t 1/2 (min)	2.2	9.7	6.5	Reaction product half-life
t_D(min)	1.5	1.5	1.5	Typical delay time between laser shot and commencement of counting
t_C(min)	5	19	13	Optimum counting time
B(cpm)	0.2-0.3	0.5-0.6	0.5-0.6	Typical preshot background rate
$[\rho\Delta R]\ Y_n$	2.0×10^4	1.5×10^4	–	Threshold pusher areal density, neutron yield product
$[\rho R]\ Y_n P_T$	–	–	3.0×10^4	Threshold fuel areal density, neutron yield, bromine fill (in atm) product

Table 1

WAVELENGTH DEPENDENT ABSORPTION

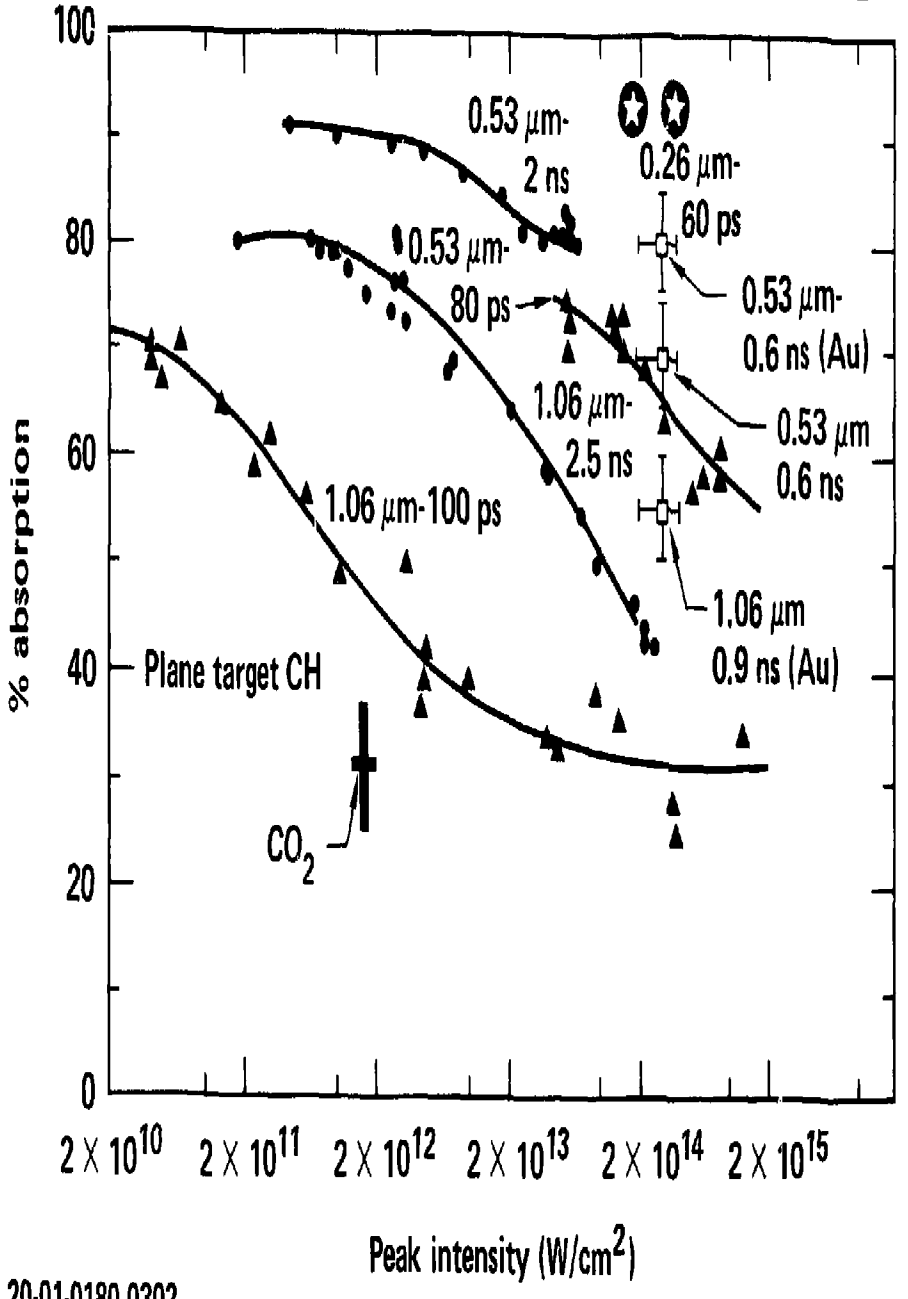

20-01-0180-0302

Figure 20

$2\omega_0$ EXPERIMENTS

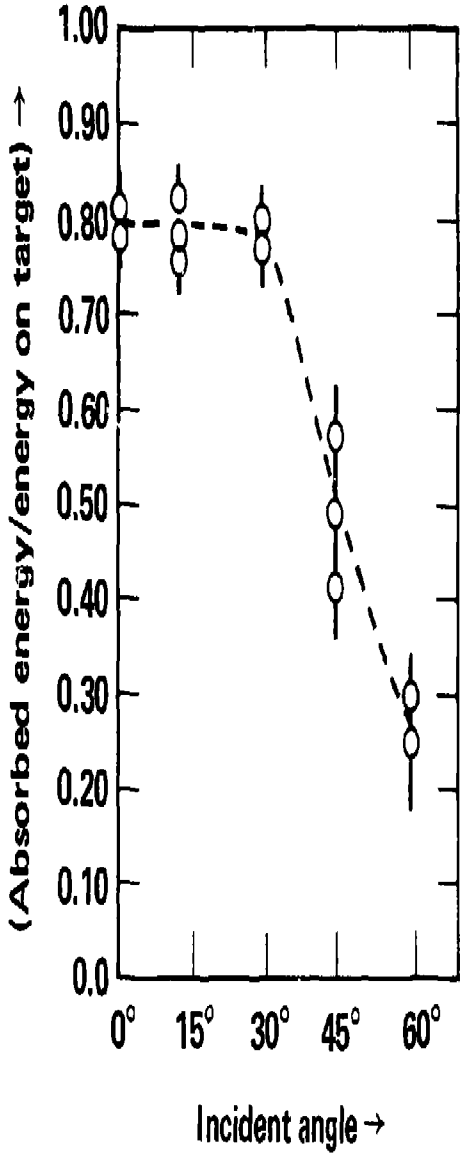

$2\omega_0$ – experiments:

Target: Gold disc

Pulse length τ (ns):

$0.49 \leqslant \tau \leqslant 0.87$

Energy on target E_{inc} (J)

$11.75 \leqslant E_{inc} \leqslant 13$

Irradiance I ($W \cdot cm^{-2}$)

$1 \times 10^{14} \leqslant I \leqslant 3.5 \times 10^{14}$

Focusing lens f/2.2

20-15-0180-0031

Figure 21

FROM THE ANGULAR DEPENDENCE OF THE MEAN RED SHIFT, THE DOPPLER AND BRILLOUIN SHIFTS CAN BE SEPARATED

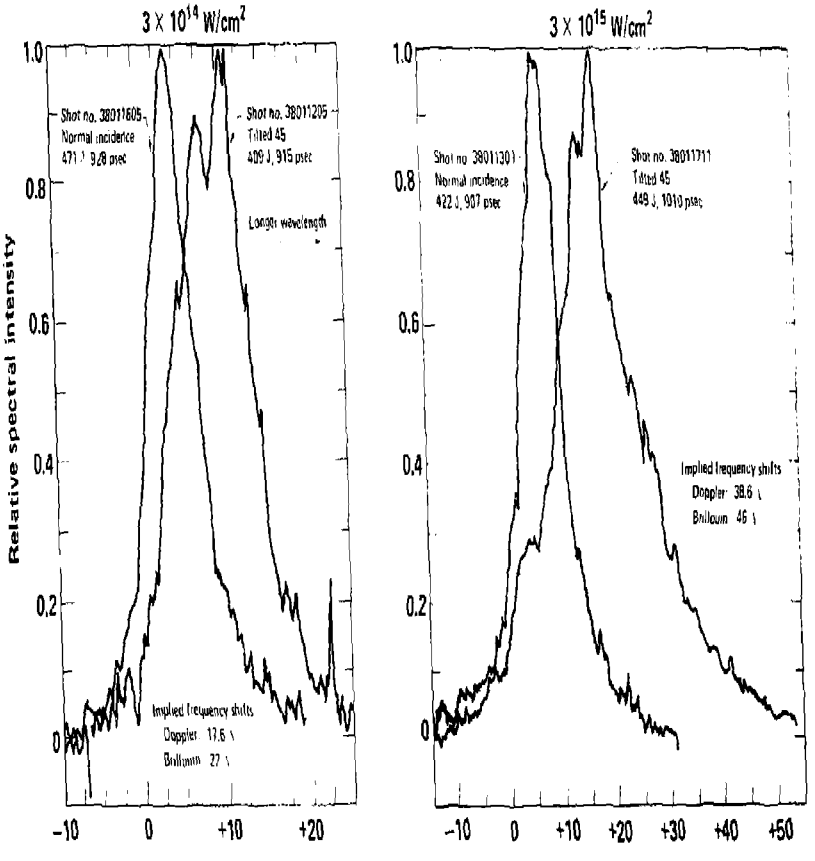

20-90-0578-1800

Figure 22

5320 Å GREEN LIGHT EXPERIMENTS SHOW THE SPECTRUM OF THE BACKREFLECTED LIGHT SHIFTING TO THE RED FOR BOTH PARYLENE AND GOLD DISKS AS THE TARGET IS TILTED

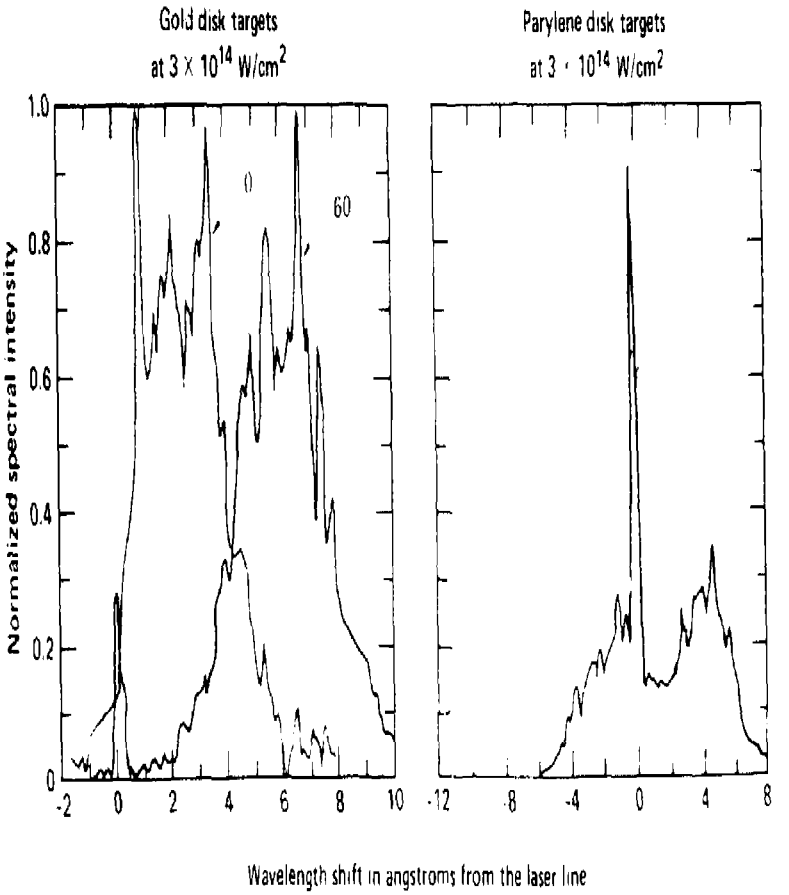

20-90-0180-0295

Figure 23

RAMAN LIGHT EXPERIMENT

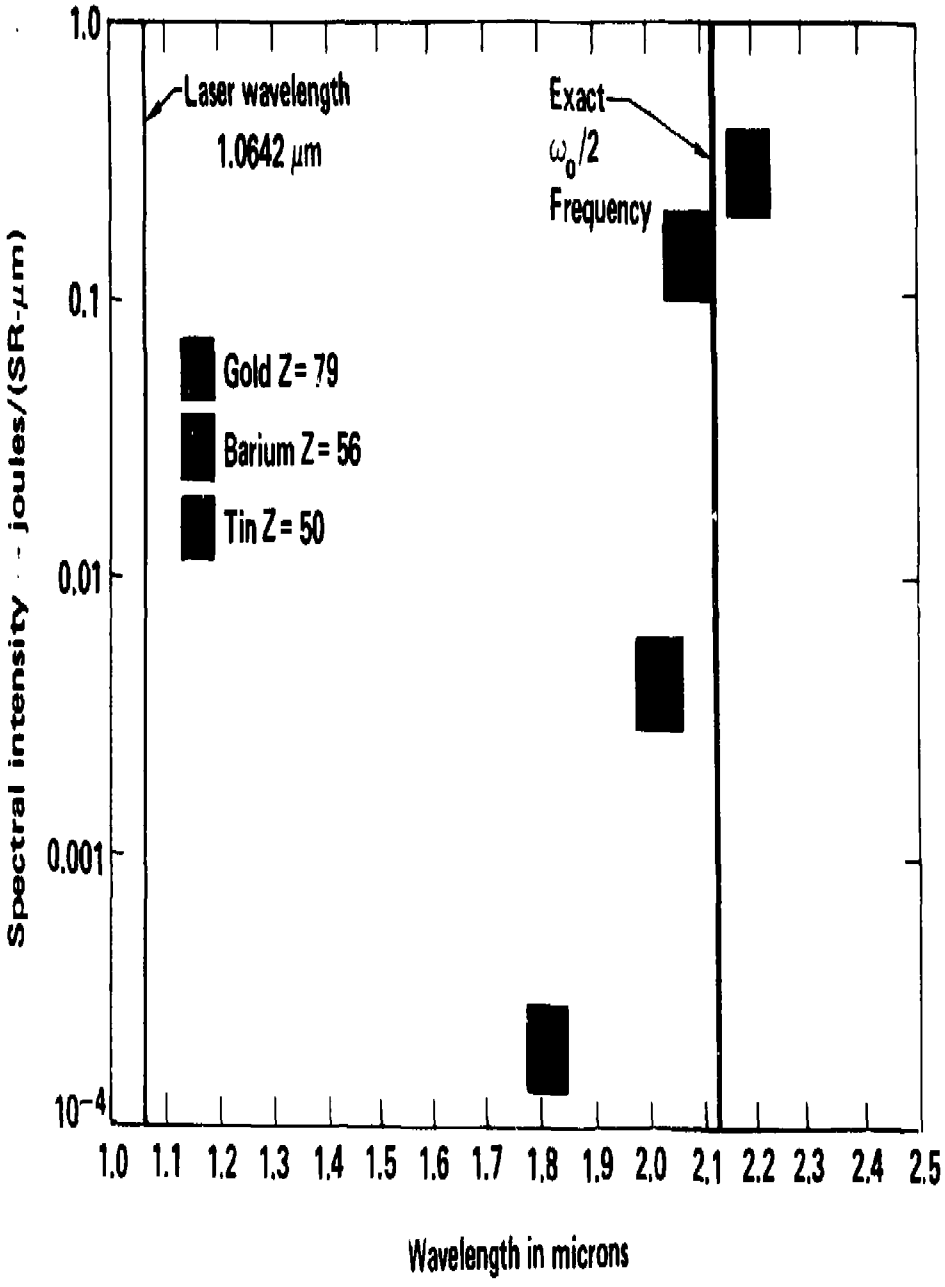

20-90-0679-1953

Figure 24

RAMAN LIGHT MEASUREMENTS
FOR GOLD DISKS IRRADIATED AT HIGH INTENSITY

Experiment description	Spectral intensity measurements			
	1.6 μm	1.8 μm	2.0 μm	2.13 μm
$\sim 10^{16}$ W/cm^2				
100 μm diam spot 600 joules in 600 psec Target tilted 30° toward the light collector	0.12 joules/ (SR-μm) IN PLANE $\Delta\theta = 5.6°$	$>$0.09 joules/ (SR-μm) IN PLANE $\Delta\theta = 7.2°$	—	0.15 joules/ (SR-μm) IN PLANE $\Delta\theta = 11.2°$
$\sim 10^{17}$ w/cm^2				
Best focus spot 900 joules in 1000 psec Targets irradiated at normal incidence	0.38 joules/ (SR-μm) IN PLANE $\Delta\theta = 25°$	0.52 joules/ (SR-μm) IN PLANE $\Delta\theta = 25°$	0.43 joules/ (SR-μm) IN PLANE $\Delta\theta = 25°$	—

20-90-1079-4402

Figure 25

RAMAN LIGHT EXPERIMENT – SHORT PULSE TRANSPORT EXPERIMENTS

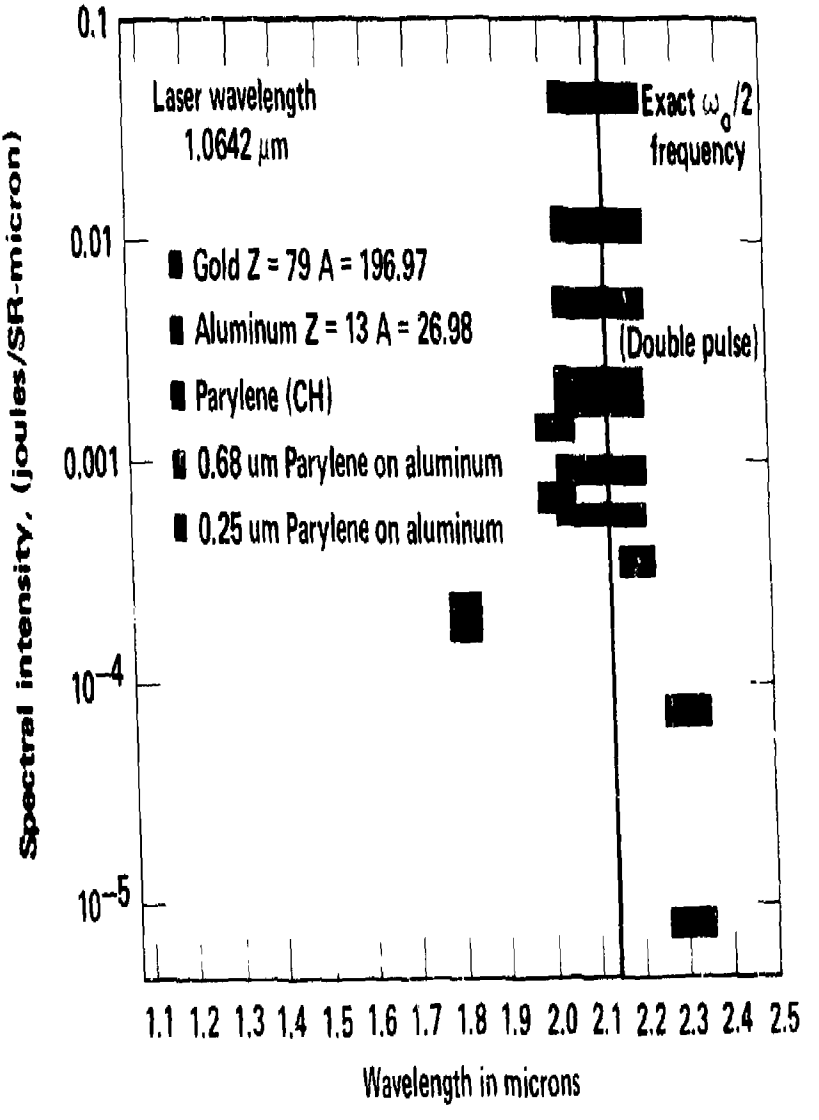

20-90-0779-2241

Figure 26

HIGH ENERGY X-RAY ANGULAR DISTRIBUTION

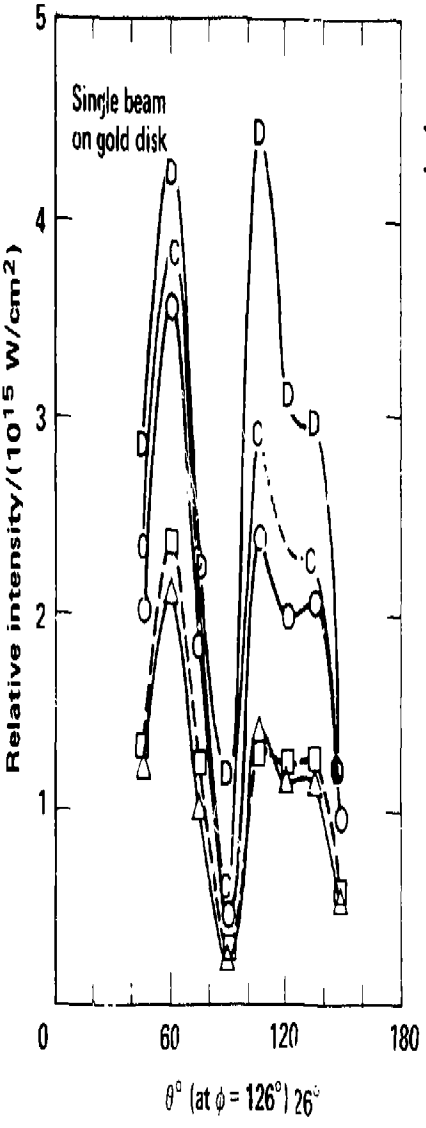

Beam	Shot no.	Energy (J)	Intensity (10^{15} W/cm^2)
— 13 □	72702	207	2.11
— 13 ○	81004	191	1.77
11 △	80914	209	2.13
17 C	80915	247	2.52
3 D	81008	219	2.03

Beam	Δφ°	Δθ° (E)
13	0	0
11	72	7.7
17	36	17.4
3	0	0

20-50-0280-0396

Figure 27

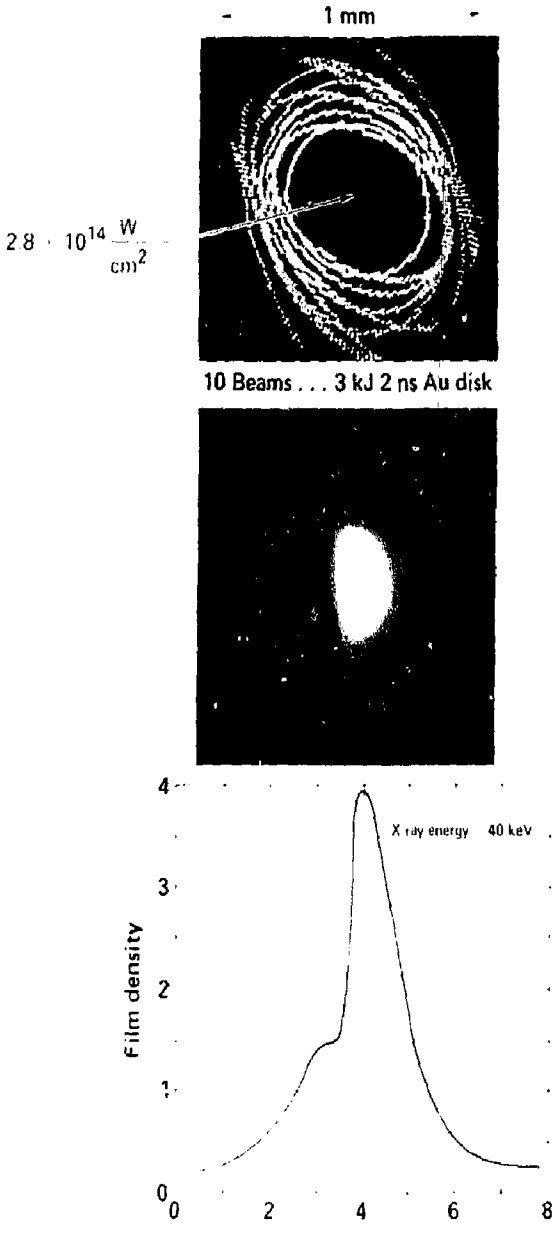

20 90-0280-0342

Figure 28

FRACTIONAL RADIATION LOSSES FROM Au DISKS

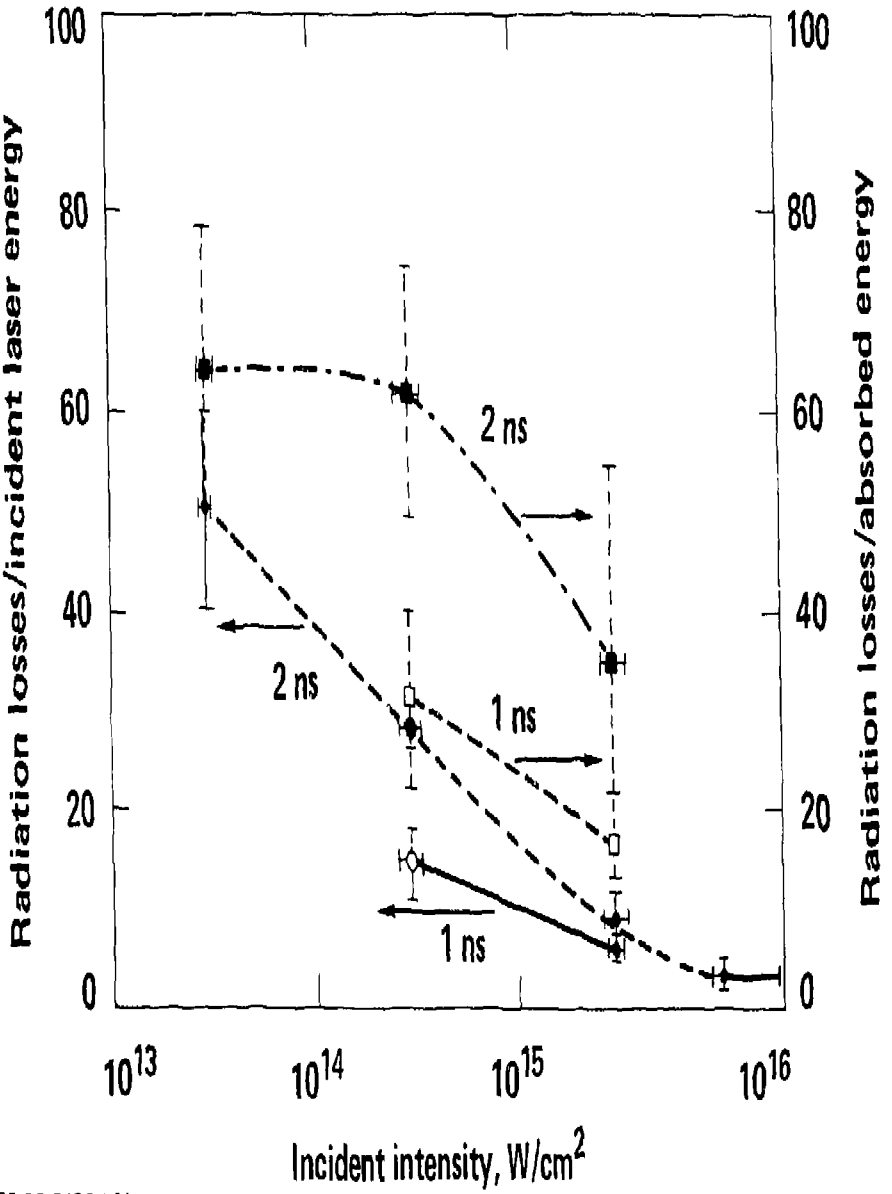

20-90-0280-0338

Figure 29

Z DEPENDENCE OF THE TIME-RESOLVED SUB-keV X-RAY EMISSION FROM LASER-PRODUCED PLASMAS

Laser

$I = 5 \times 10^{14}$ W/cm^2

1 ns FWHM

XRD

520 eV channel

190 ps resolution

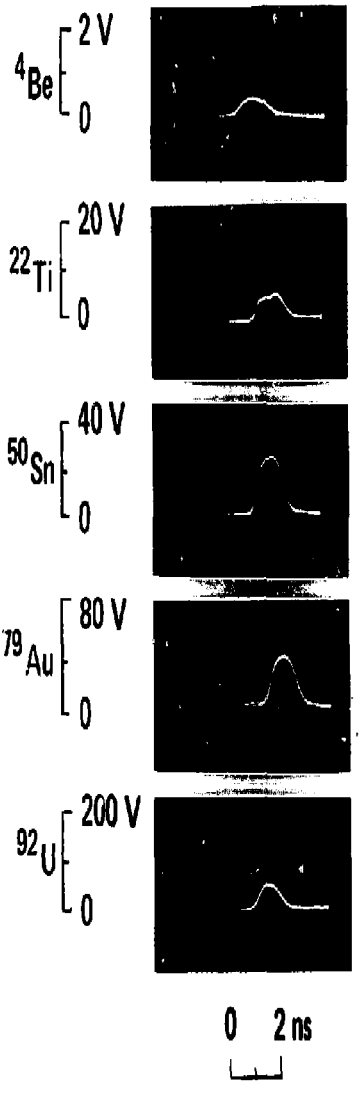

20-50-0679-1864

Figure 30

TIME-RESOLVED SUB-keV X-RAY EMISSION FOR Au-DISKS AT DIFFERENT LASER INTENSITIES (XRD: 940 eV CHANNEL, 170 ps RESOLUTION)

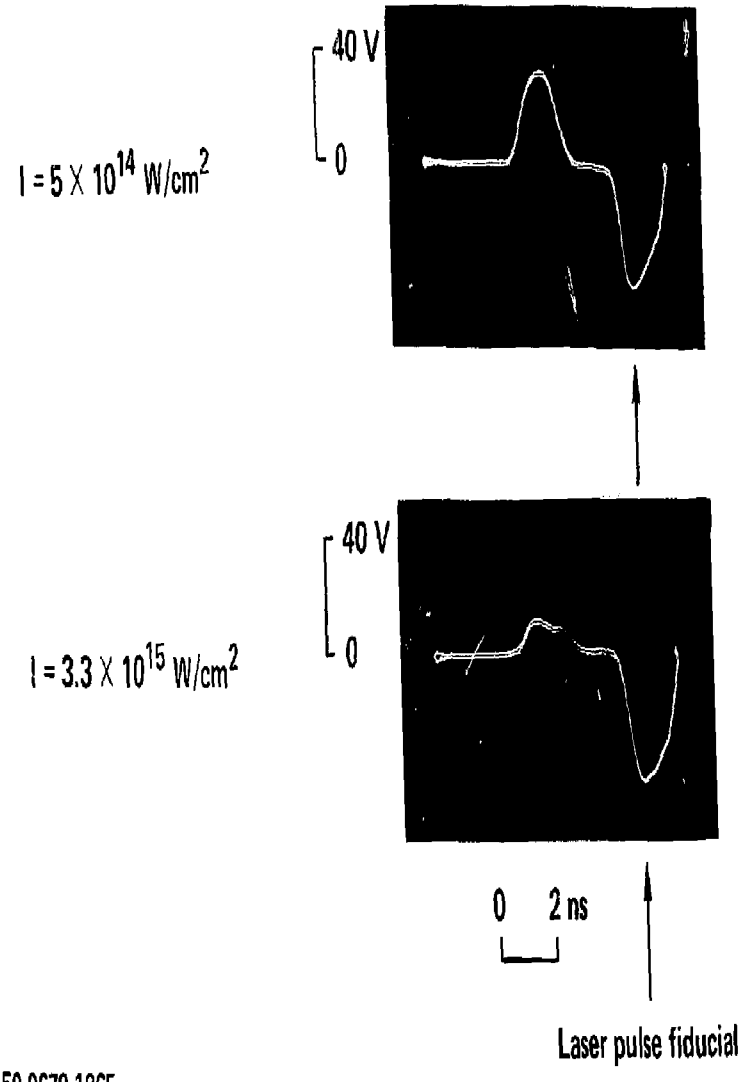

20-50-0679-1865

Figure 31

EXPLODING PUSHER IMPLOSION

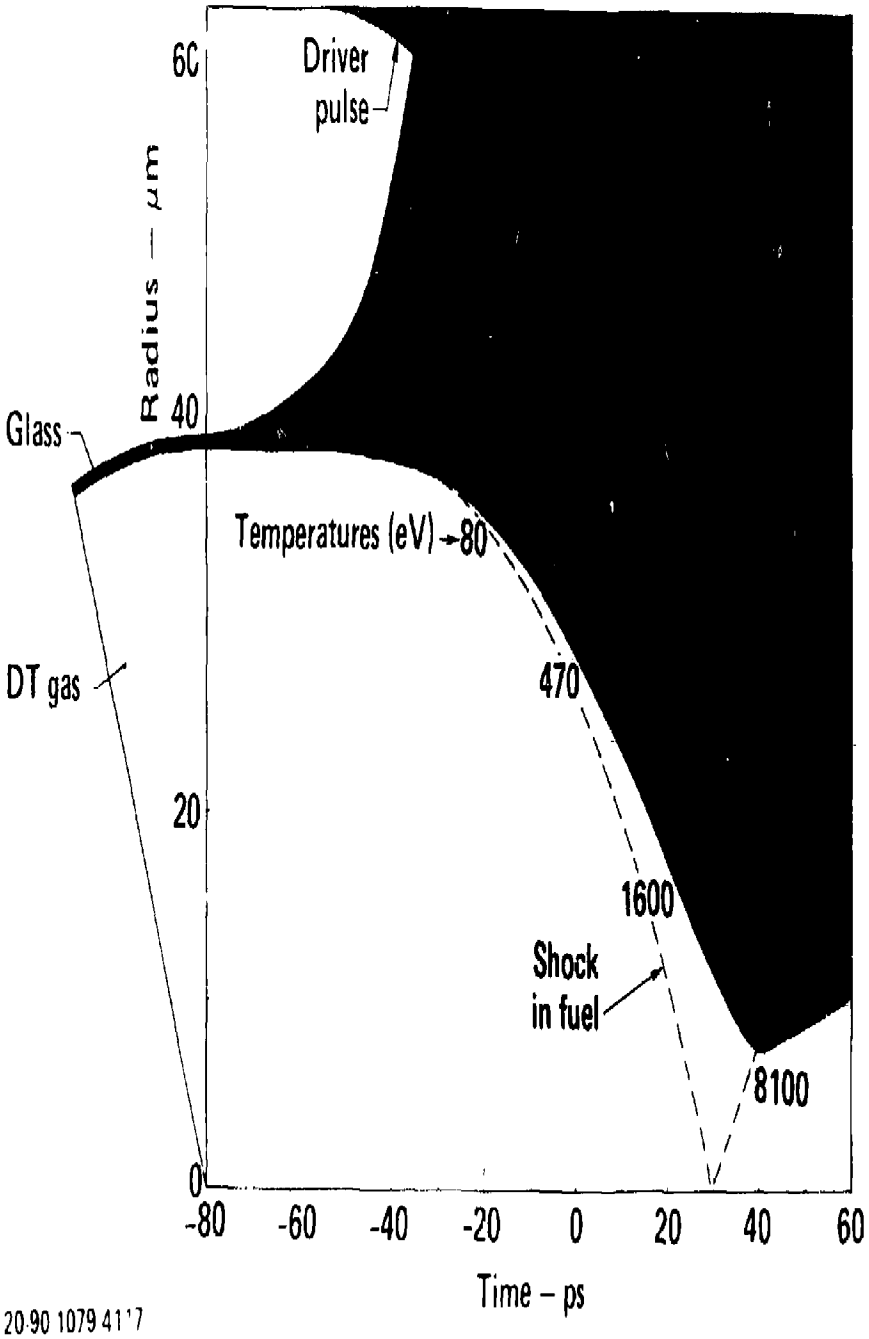

20-90 1079 41'7

Figure

ABLATIVE IMPLOSION

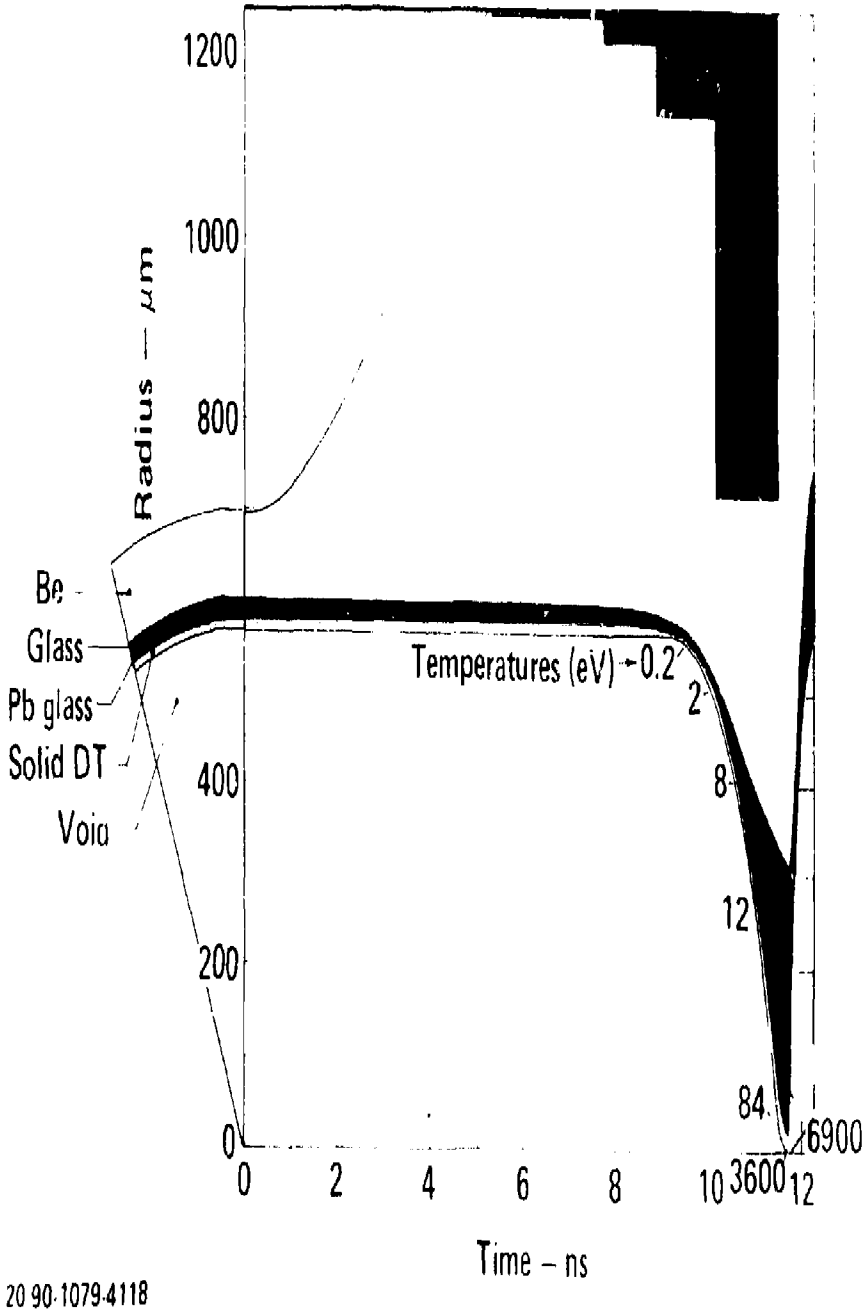

20 90-1079-4118

Figure 33

IMPLODED TARGET CONDITIONS

Exploding pusher

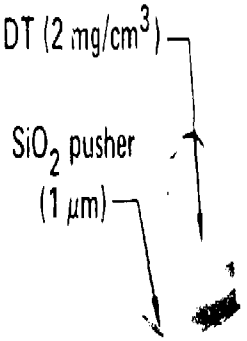

Initial inner diameter ~ 300 μm

20-30 TW
100 ps

T_i ~ 4-8 keV

ρ_{DT} ~ 0.1 g/cm^3

Ny ~ 10^9-10^{10}

$T_e \sim T_i$

$(\rho\Delta R)_{pusher}$ $5 \cdot 10^{-4}$ g/cm^2

Intermediate density

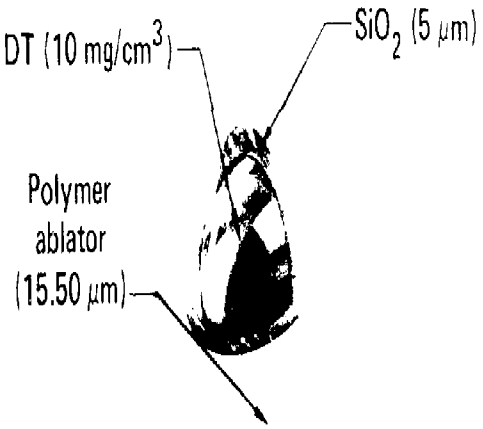

Initial inner diameter ~ 140 μm

20 TW
200 ps

T_i ~ 0.5-1 keV

ρ_{DT} ~ 2-5 g/cm^3

Ny ~ 10^7-10^9

$T_e \gtrsim T_i$

$(\rho\Delta R)_{pusher}$ ~ $1{\cdot}2 \cdot 10^{-2}$ g/cm^2

20 90 1079 4091

Figure 34

HIGH ENERGY X-RAY EMISSION SUGGEST $T_{hot} \sim 30$ keV, $f_{hot} > 0.5$

- Significant uncertainty: angular emission modulation

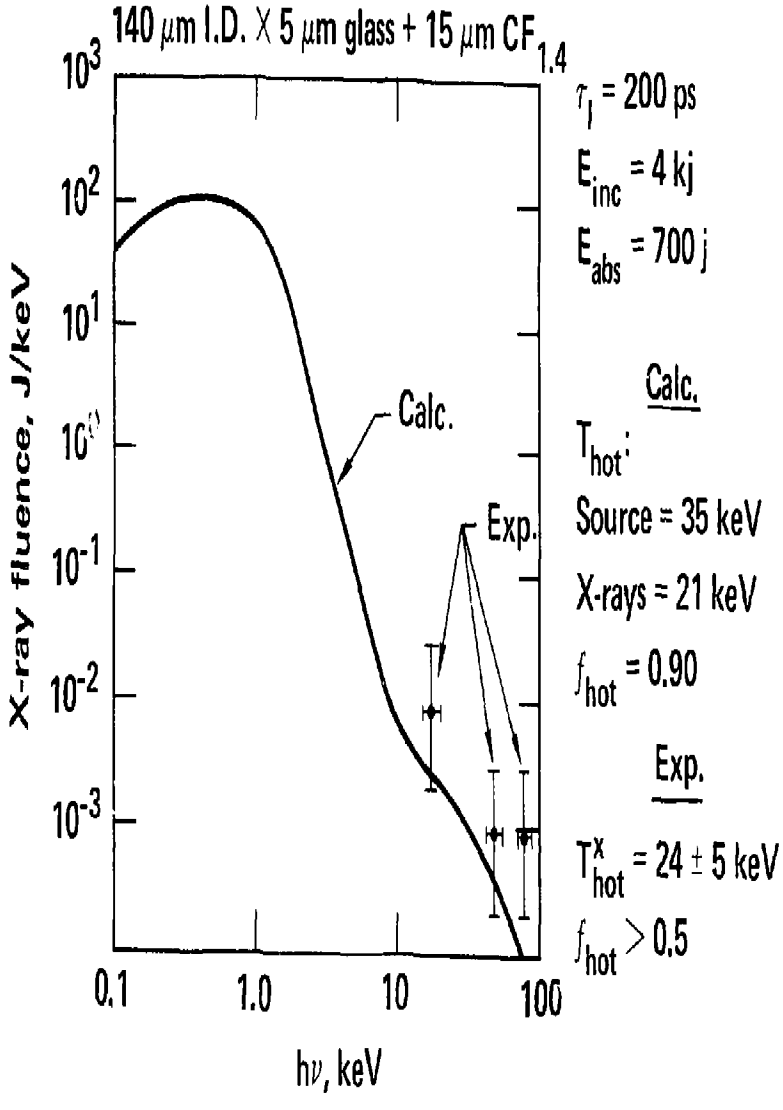

50-60-1079-4351

Figure 35

RADIUS VS TIME FOR "10X" BALL TARGET SHOWS EARLY ABLATION FOLLOWED BY PUSHER DECOMPRESSION

- A "swelling pusher" implosion

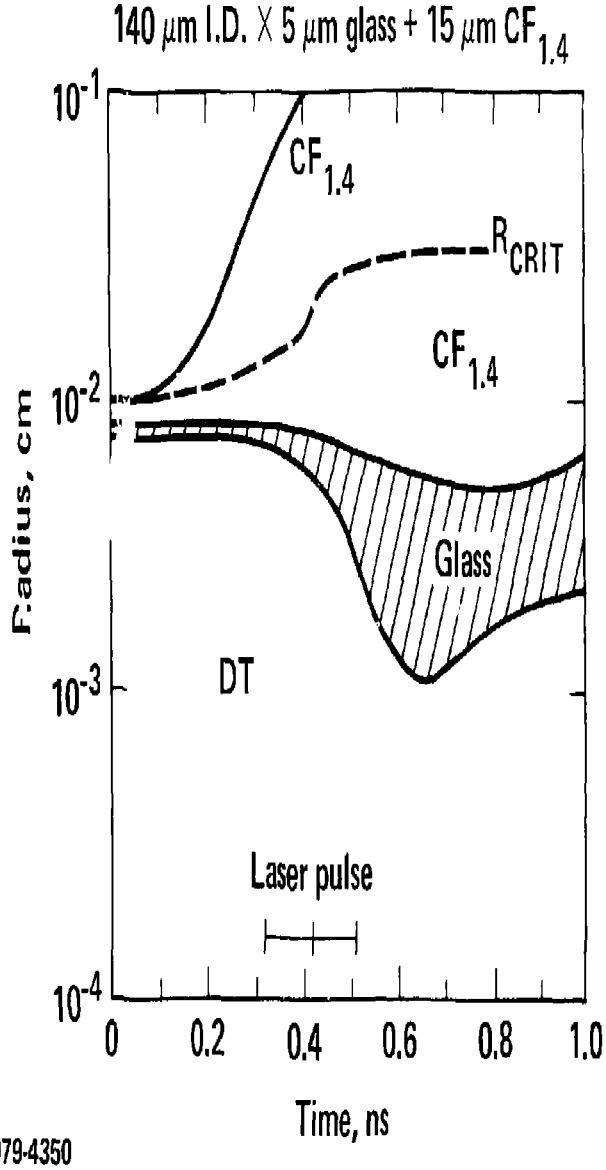

50-60-1079-4350

Figure 36

DT ADIABATS FOR 10 - 100X TARGET DESIGNS

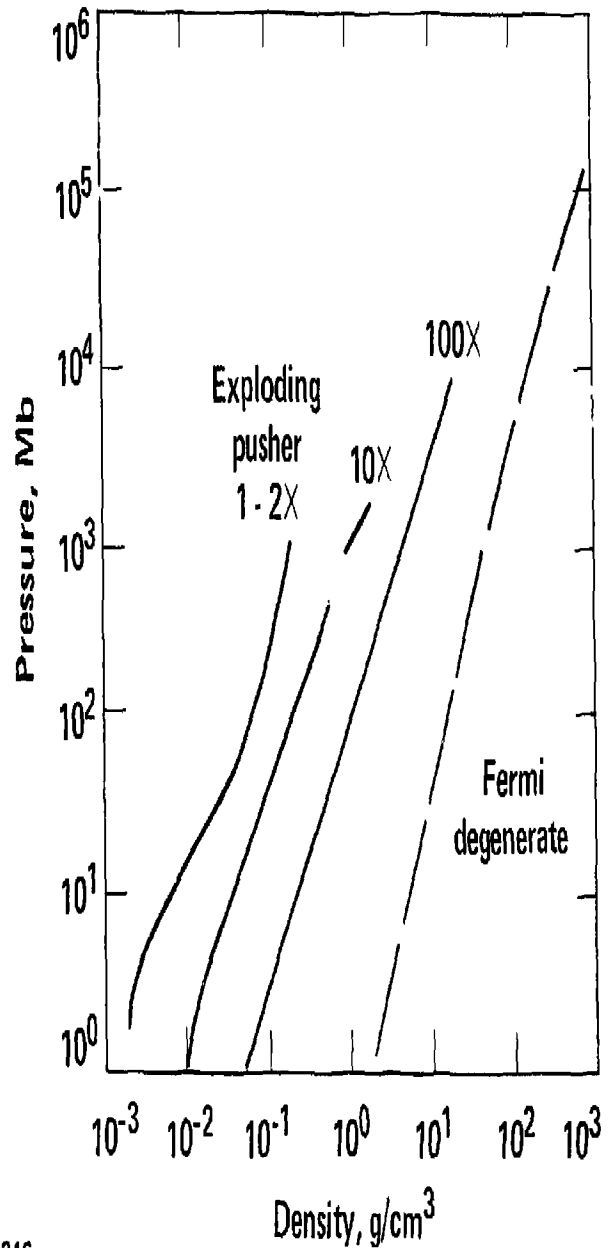

50-60-1079-4346

Figure 37

10X LIQUID DENSITY EXPERIMENTS

Measurement Summary

140 X 5 + 15 CF balls τ = 200 psec FWHM

Shot no.	Laser energy	Neutron yield	Radiochemistry pusher ($\rho\Delta R$) aff (G/cm^2)	X liquid density		Argon line FWHM (μm)	X liquid density	
				ρ_{DT} simple model	ρ_{DT} simulation		ρ_{DT} (argon line imaging)	
							Sphere	2:1 ellipsoid
89071706	1.99 kJ	$(1.56 \pm 0.22) \times 10^7$				50 ± 10	5 ± 2	1.3 ± 0.4
89072310	4.10 kJ	$(6.7 \pm 0.6) \times 10^8$	0.0059 ± 0.0015	5^{+2}_{-2}	$^{PC}18^{+8}_{-7}$ $^{PB}9^{+4}_{-5}$			
89072513	3.48 kJ	$(1.30 \pm 0.14) \times 10^8$	0.0047 ± 0.0022	4^{+2}_{-2}	$^{PC}13^{+10}_{-7}$ $^{PB}6^{+6}_{-4}$	20 ± 5	23 ± 9	6^{+3}_{-3}
89073104	4.10 kJ	$(6.5 \pm 0.7) \times 10^8$				35 ± 5	5 ± 2	1.3 ± 0.4
89073106	3.96 kJ	$(3.5 \pm 0.4) \times 10^8$	0.0063 ± 0.0018	6^{+3}_{-2}	$^{PC}19^{+11}_{-6}$ $^{PB}10.5^{+7.5}_{-5.5}$	35 ± 5	5 ± 2	1.3 ± 0.4

PB = peak burn PC = peak compression

20-90-0180-0257

Table 2

COMPRESSION DIAGNOSTICS ARE SENSITIVE TO SPACE AND TIME DEPENDENCE OF TEMPERATURE AND DENSITY:

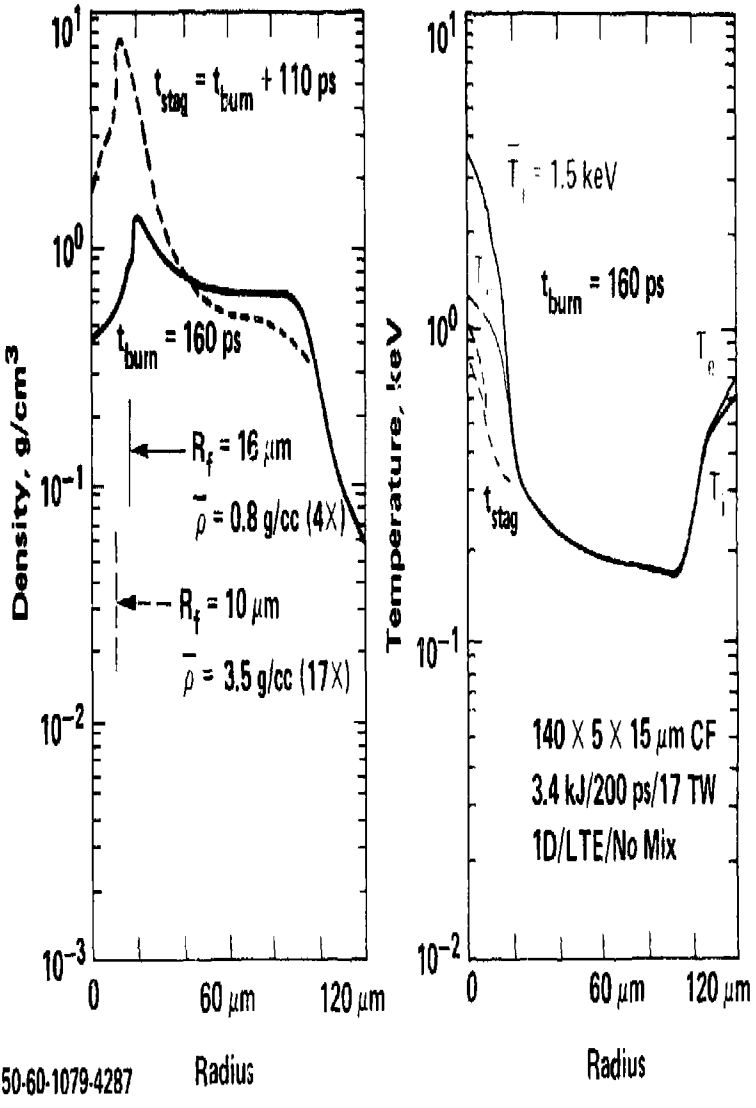

50-60-1079-4287

Figure 38

RESULTS OF SENSITIVITY STUDY SHOW ρ_F CAN BE INFERRED FROM $(\rho\text{-}\Delta R)_p$ WITH ~ 2X UNCERTAINTY

140 μm I.D. X 5 μm glass + 15 μm $CF_{1.4}$, 0.01 g/cm^3 DT fill

τ_L = 200 ps

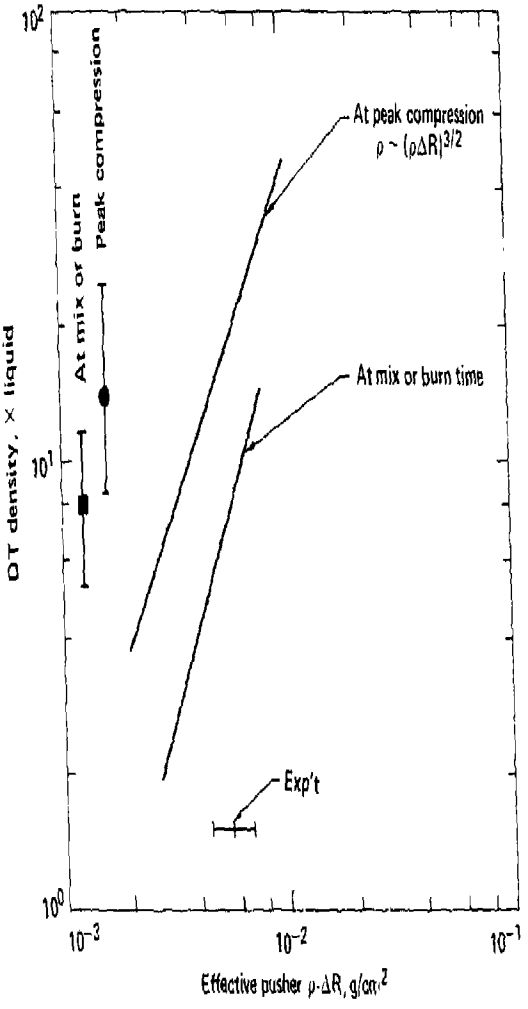

50-60-1079-4562A

2/80

Figure 39

X RAY IMAGE DEMONSTRATES FUEL COMPRESSION TO 10 · LIQUID DT DENSITY

Images at 'high' energy (5 10 keV) are required to see through the high density glass to the fuel region

6.5 keV

Shot: (89072310)-1R3

6.5 keV x ray image clearly shows the compressed fuel pusher interface

40 90 0280 0298

Figure 40

FUEL DENSITY AT BURN TIME VERSUS NEUTRON YIELD

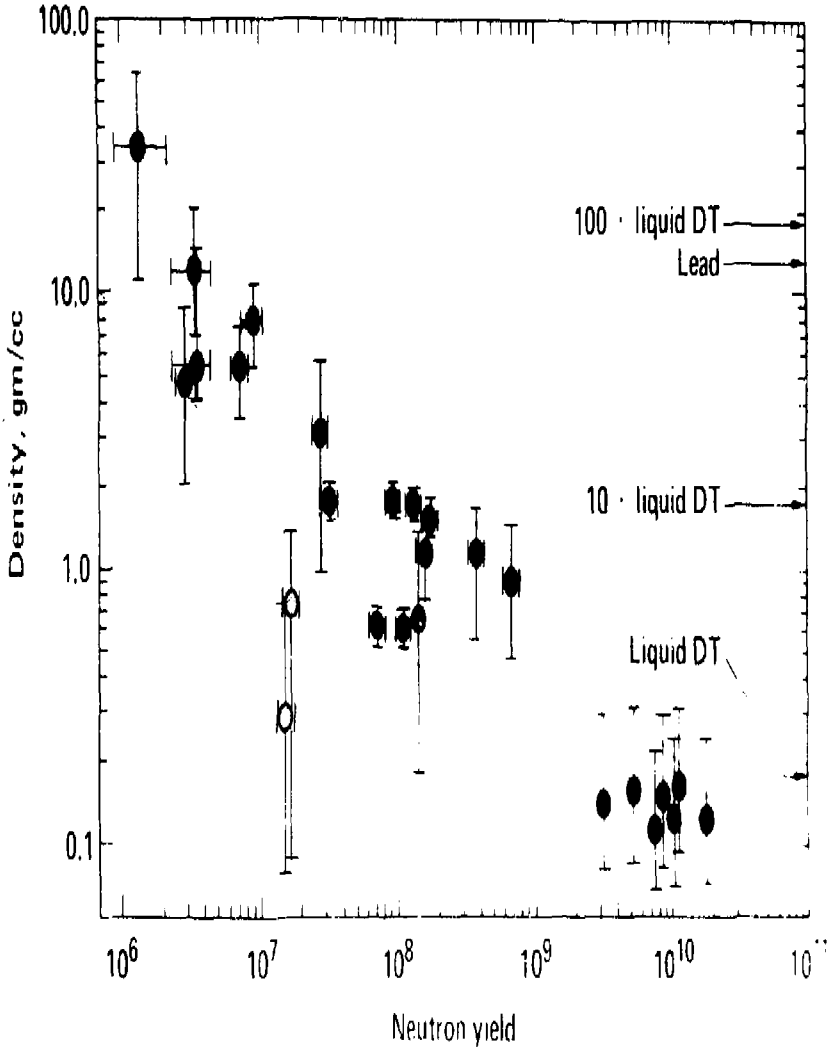

20-15-0579-1728A

Figure 41